university of groningen

faculty of science and engineering

Discovering SO_2 in JWST MIRI MRS spectra of protoplanetary disks

Author:
Thomas SMEMAN
(s4950836)

Supervisor:
prof. I. E. E. (Inga) KAMP
Second examiner :
prof. dr. F. F. S. (Floris) VAN DER TAK

December 9, 2024

Contents

Abstract

The sulfur depletion problem describes the fact that only 1% of the theoretical total sulfur abundance in protoplanetary disks is observed. Using JWST MIRI MRS observations of protoplanetary disks, SO_2 could be used as a tracer for the total sulfur abundance. Using local thermal equilibrium slab models made with ProDiMoPy and an observed debris disk as a template for a typical noise profile, a cross-correlation method is developed to observe SO_2 in various scenarios. The technique retrieves SO_2 from mock spectra consisting of the aforementioned debris disk, with an SO_2 spectrum added in at various signal-to-noise ratios. The estimates have high precision in both temperature and column density, but lose accuracy when adding other species to the simulated spectra. By comparing the spectrum with a slab model spectrum of the best estimate of column density and temperature for a given emitting radius, visual confirmation of SO_2 detection can be obtained. The method was applied to GWLup, but no SO_2 could be detected, meaning any SO_2 emission will be below a signal-to-noise ratio of 2. There are few possibilities for temperature and column density combinations that achieve this value, with a requirement of a large emitting area, meaning there are no likely scenarios for GWLup to contain SO_2 detectable with this method. Obtaining the signal strength with a high column density would require a value around 10^{17} cm^{-2}, which is unlikely based on previous estimates in literature.

Acknowledgments

I would especially like to thank my supervisor, prof. Inga Kamp, for guiding me throughout my research project and giving me some much needed guidance, as well as Aditya Arabhavi and Jelke Betlehem for giving some useful insights. I am thankful for prof. dr. Floris van der Tak to agree to be the second reader for my thesis. I thank the Center for Information Technology of the University of Groningen for their support and for providing access to the Hábrók high performance computing cluster. Lastly, a big thanks to my friends for providing the support I needed and for the rubber ducking that helped me get this far.

1 Introduction

Sulfur is a relatively abundant element on Earth, ranking as the 16th most abundant element on the planet and the 10th most abundant in the galaxy [1]. It is a vital component of various amino acids, including cysteine ($C_3H_7NO_2S$) and methionine ($C_5H_{11}NO_2S$), which are crucial for life and habitability. This suggests that sulfur was present in the protoplanetary disk (PPD) when Earth formed [2]. However, sulfur is notably absent in observations of the inner 10 AU of PPDs, where terrestrial planets form. The sulfur-bearing species identified in the outer regions ($>$ 10 AU) account for only about 0.1% of sulfur's estimated cosmic abundance ($1.23 \times 10^{-5} n_H$) [1, 3].
Several theories have been proposed to explain this discrepancy. One hypothesis suggests that sulfur is sequestered in previously overlooked molecules, such as allotropes [2]. Another posits that sulfur resides in icy grain mantles or polymeric species formed on dust grains after photodissociation of sulfur allotropes [3]. This mechanism is believed to address the low sulfur abundances observed in dense molecular clouds and PPDs.
Approximately 90% of sulfur in PPDs is thought to be locked in refractory materials, which resist decomposition by heat [2]. In dense molecular clouds, only 0.6-6% of the cosmic sulfur abundance is found in SO_2 [4]. In these environments, only five sulfur-bearing species have been identified: CS, SO, H_2S, H_2CS, and SO_2. Together, these account for only about 1% of the total solar sulfur abundance, leaving the sulfur-bearing species in the inner regions of PPDs largely unexplained [2]. Thus, a key question arises: In which molecules is sulfur locked? One theory suggests that sulfur allotropes, which are stable in nature, may form on dust grains through surface chemistry, as their gas-phase formation is inefficient [2]. Observations by ALMA (Atacama Large Millimeter/submillimeter Array) have the sensitivity to detect certain sulfur-bearing species such as OCS, but so far, only CS and SO_2 have been detected in the protoplanetary disk of DM Tau [5]. The inability to identify sulfur's primary reservoirs in PPDs is known as the sulfur depletion problem.
The James Webb Space Telescope (JWST) offers an opportunity to gain further insight into this issue. Using the Mid-Infrared Instrument (MIRI), JWST provides spatially resolved medium-resolution spectroscopy (MRS) data between 4.9 μm and 27.9 μm. In this study, we utilize MRS spectra of PPDs to search for SO_2 emission. As a test case, model spectra are generated using ProDiMo and adjusted to match JWST observation capabilities. The resolving power ($\lambda/\Delta\lambda$) of this instrument ranges from approximately 1550 to 3250 [6, 7]. This thesis aims to address two key questions: Can SO_2 be detected in protoplanetary disks using JWST MIRI spectra? If so, can the temperature and column density of SO_2 be determined from these spectra?
This thesis is structured as follows: First, we provide background information on protoplanetary disks and the rationale for using SO_2 as a tracer for sulfur abundance. Next, we describe the theoretical framework, including the physics of emission lines, the ProDiMoPy modeling software, and the JWST MIRI MRS instrument. We then detail the methodology for identifying sulfur in spectra, including the steps taken to refine and validate the approach. Subsequently, we apply the method to a spectrum of the protoplanetary disk GWLup and discuss how SO_2 can inform estimates of the total sulfur abundance. The results section presents our findings, and finally, we outline the limitations and potential improvements to the method.

2 Background Literature

2.1 Protoplanetary Disks

Protoplanetary disks (PPDs) are gas-rich disks around young stars. These disks can contain dust and also can potentially form planets, as well as contain them. The chemical compositions of these disks can thus dictate the compositions, locations, evolutions, and orbital configurations of planets, as well as influence many other properties of the disk [8, 9]. Especially in the inner 0.1 to 10 AU region of a PPD, terrestrial planets can form around low-mass (less than 2 solar masses [10]) stars. This region has relatively high temperatures of over 100 K and has high densities of over 10^8 cm^{-3} [11]. However, planets form only in a short time window of less than 10 million years [9].

2.1.1 Origin and Composition

PPDs form during star formation, when interstellar cloud material gets distributed in a disk-like structure to preserve angular momentum. Many volatile molecules from the interstellar medium are contained within stable molecules such as H_2, CO, CO_2, N_2, NH_3, and H_2O. The clouds can also produce first-generation organic molecules, such as methane (CH_4) and methanol (CH_3OH) [8].
From Spitzer-IRS observations including the molecules H_2O, OH, HCN, C_2H_2, and CO_2 combined with Keck-NIRSPEC observations for CO emission of PPDs, some column densities for the gases can be estimated. It is found that H_2O line fluxes correlate with the mid-IR continuum flux and some other factors. However, local thermal equilibrium (LTE) models suggest that in planet-forming regions, the column densities cover only a small range, where H_2O is estimated around 10^{18} cm^{-2} around 450 K. HCN estimates are around 10^{14} to 10^{15} cm^{-2} between 600 and 800 K. For C_2H_2, the column densities are in the same range, but the emission occurs more between 500 and 1200 K. For CO_2 the temperatures are the same, but the number densities range from 10^{14} to 10^{16} cm^{-2}. OH best fits a temperature range of 900 and 1100 K with number densities around 10^{15} cm^{-2}, but other experiments found number densities of up to 10^{17} cm^{-2}. CO was found to be between 10^{18} and 10^{19} cm^{-2} with typical temperatures of 900–1500 K [12].
For NH_3 and SO_2, the steps to find estimates for the column densities are slightly more elaborate, as clear results are not available in literature. However, if we assume these to be the only nitrogen and sulfur-bearing molecules, their column densities will be proportional to those of N and S respectively. The relative abundances on the scale of $\log n_H = 12$ are 7.90 for nitrogen, 8.48 for oxygen and 5.27 for sulfur, which means $n_N = 10^{7.90-12}$, $n_O = 10^{8.48-12}$ and $n_S = 10^{5.27-12}$ relative to hydrogen [13]. We then have to convert these values to relative to water, which will result in $n_{NH_3} \approx 10^{17}$ to 10^{18} cm^{-2} and $n_{SO_2} \approx 10^{14}$ to 10^{15} cm^{-2}, assuming nearly all nitrogen and sulfur is locked in these molecules.

2.1.2 Models of PPDs

The models shown are derived from [14, 15] and explained in appendix A.1, where first a radial model is derived, followed by a model including vertical variations. The purpose of this is to understand what a protoplanetary disk would look like for given parameters in terms of temperature and surface densities. Figures 1 and 2 show the disk in two ways when only considering radial variation. Figures 3 and 4 apply the same visualization techniques but using the model that includes both vertical and radial dependence in its parameters. The graphs visualize each quantity as a function of radius, while the other figures give a clearer insight into the total shape of the disk. All figures are for a 1 $M_\odot$ star, with a constant accretion rate of 10^{-8} $M_\odot$/yr, a viscosity parameter $\alpha = 10^{-2}$, a temperature at $r_{\min}$ of

280K, a temperature power law exponent $q = 0.75$, $r_{\min} = 1$ AU, $r_{\max} = 10$ AU and a mean molecular weight $\mu = 2.3$, appropriate for a molecular gas.

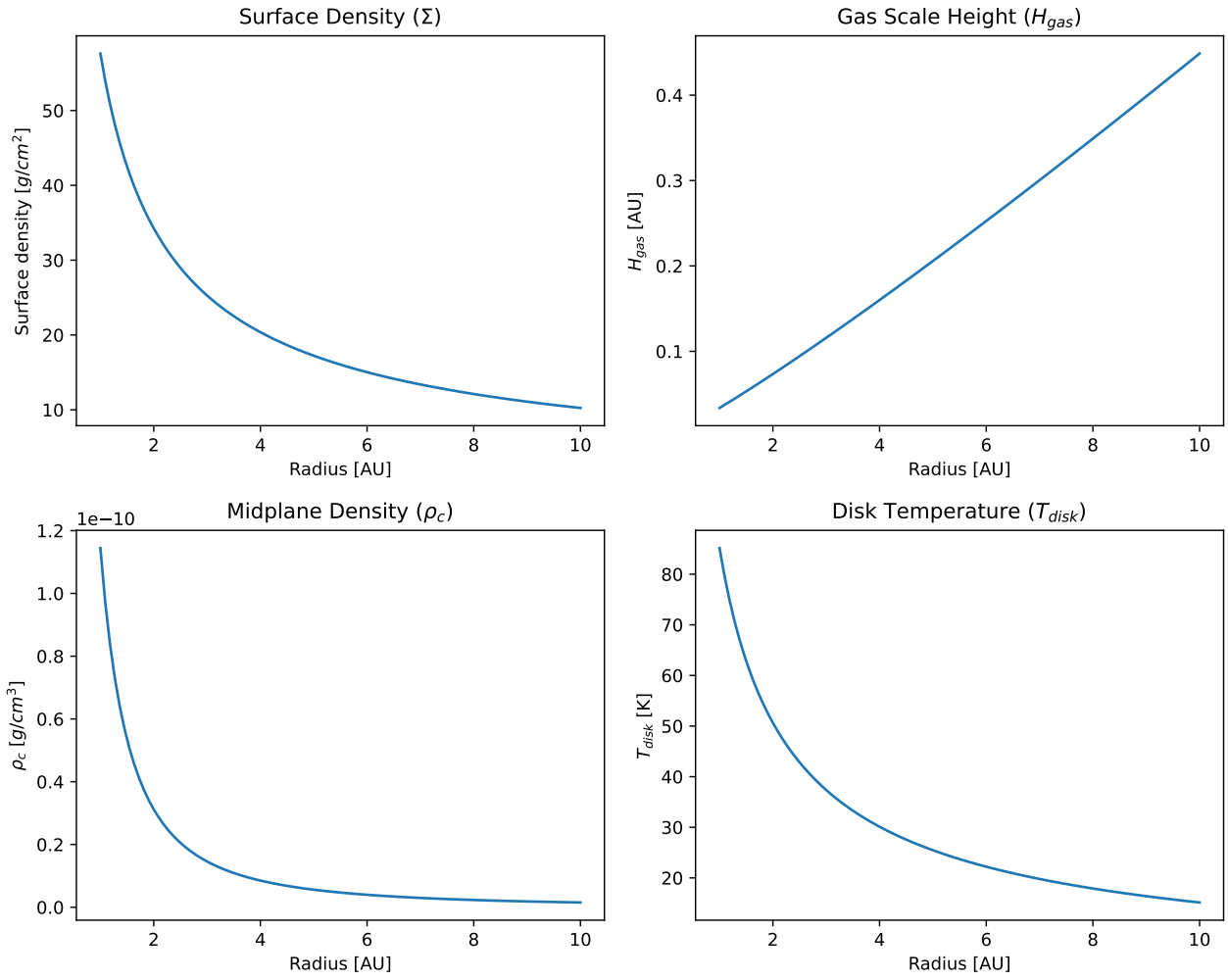

Figure 1: The top-left subplot shows the surface density against the distance from the host star in the radial direction. The top right shows the scale height H_{gas} against the radius. The bottom left shows the midplane density and the bottom right shows the disk temperature.

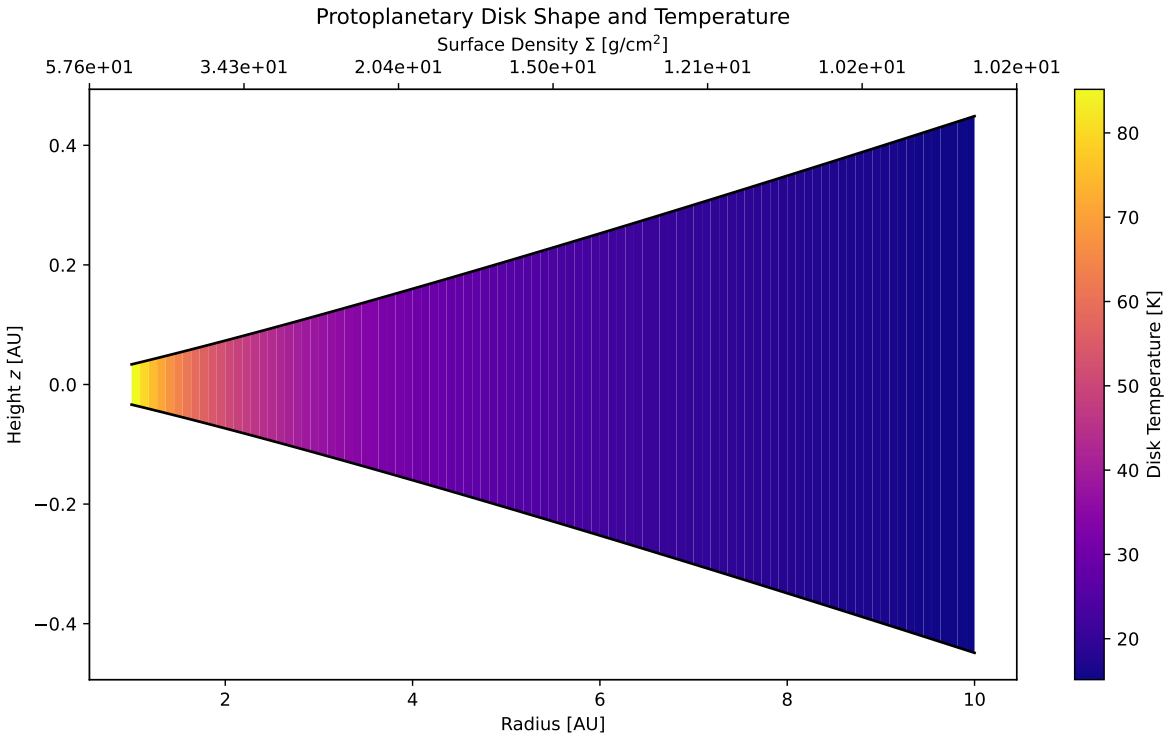

Figure 2: A symmetric model of a protoplanetary disk structure around a 1 solar mass star, modeled based on a steady-state viscous disk approximation. The x-axis shows the radial distance from the host star in AU, the y-axis shows the vertical height in AU, scaled to the gas scale height, for which the ideal gas law is assumed. The disk is assumed symmetrical around its midplane. The shaded region thus visualizes the thickness of the disk, with the color map indicating the temperature of the disk. A midplane temperature power law, $T_c \propto r^{-q}$ is assumed and the temperature is assumed constant along the vertical direction. The disk is in hydrostatic equilibrium. The viscosity is parametrized by alpha-prescription, and the accretion rate is assumed constant. The surface density $\Sigma(r)$ is derived from the steady-state solution of angular momentum conservation, assuming a Keplerian rotation profile. The surface density follows a power law dependent on the midplane temperature and radial distance. The disk is assumed optically thick and viscous heating dominates the thermal structure of the midplane.

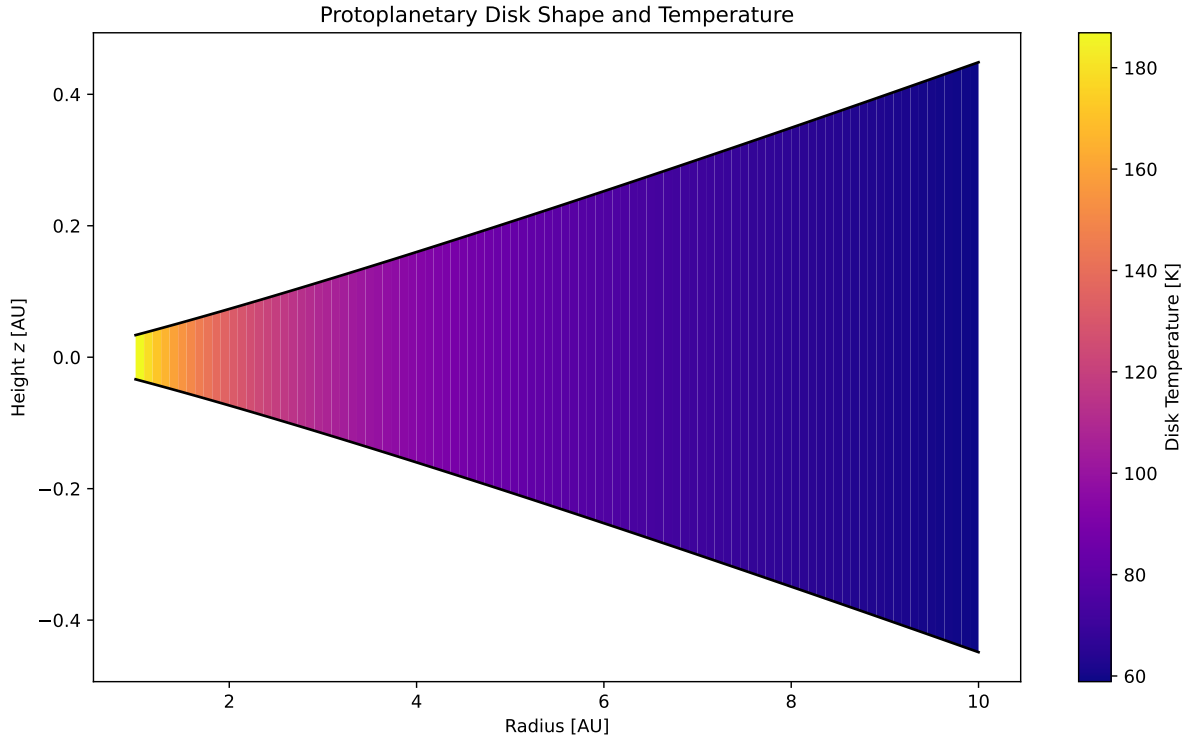

Figure 3: A symmetric model of a protoplanetary disk structure around a 1 solar mass star, modeled based on a steady-state viscous disk approximation. The x-axis shows the radial distance from the host star in AU, the y-axis shows the vertical height in AU, scaled to the gas scale height, for which the ideal gas law is assumed. The shaded region visualizes the thickness of the disk, with the color map indicating the temperature of the disk. A midplane temperature power law, $T_c \propto r^{-q}$ is assumed and the temperature is evolved in the vertical direction taking into account accretion and irradiation by the host star. The viscosity is parametrized by alpha-prescription, and the accretion rate is assumed constant. The surface density $\Sigma(r)$ is derived from the steady-state solution of angular momentum conservation, assuming a Keplerian rotation profile. The surface density follows a power law dependent on the midplane temperature and radial distance, where vertical variations are taken into account for the density computation. The disk is assumed optically thick and viscous heating dominates the thermal structure of the midplane.

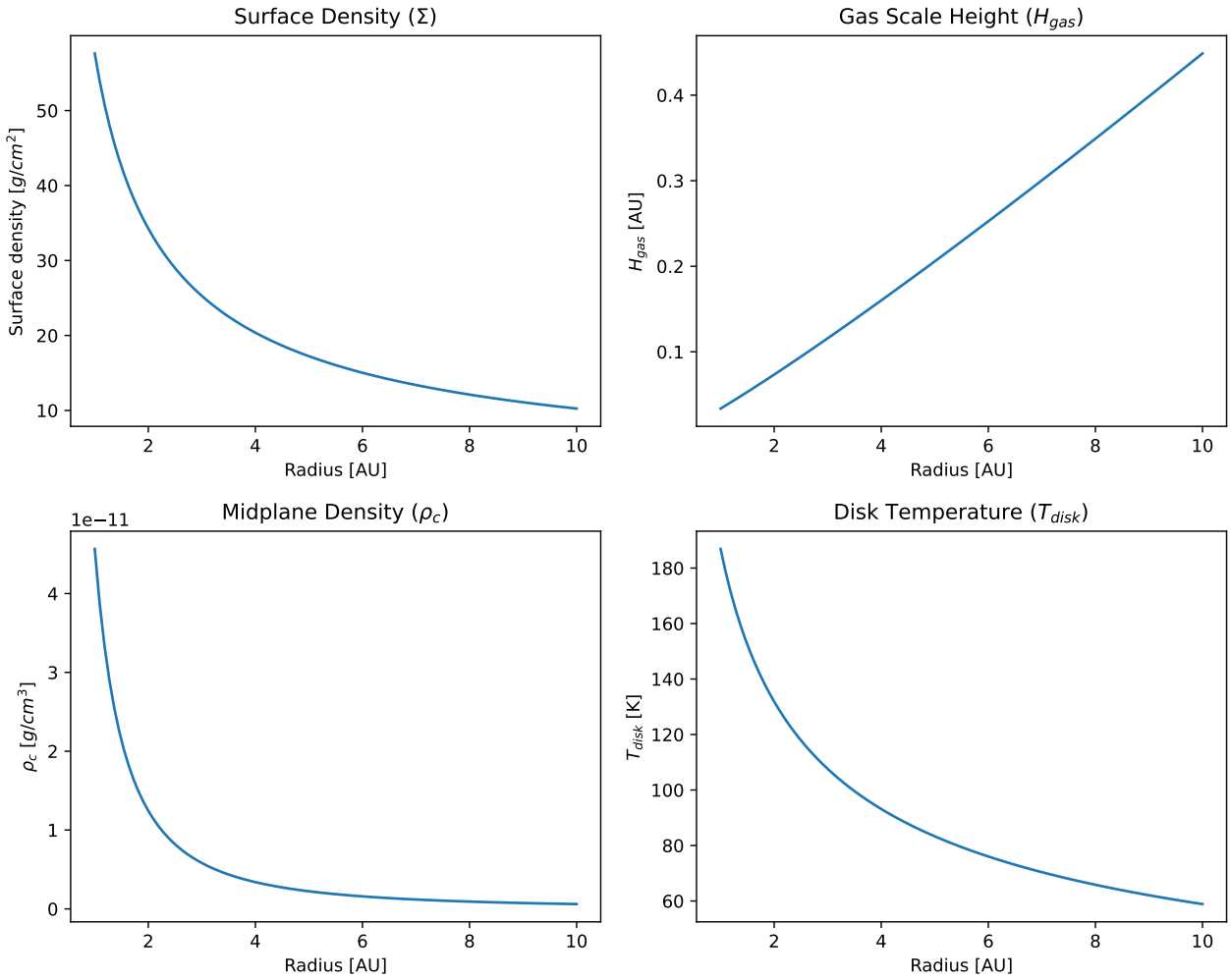

Figure 4: The top-left subplot shows the surface density against the distance from the host star in the radial direction. The top right shows the scale height H_{gas} against the radius. The bottom left shows the midplane density and the bottom right shows the disk temperature. This model assumes vertical variations for all quantities.

2.2 GW Lup

One example of such a protoplanetary disk is the disk around GW Lup. GW Lup is a young M1.5-type star with an effective temperature $T_{\text{eff}} = 3630\,\text{K}$, a luminosity of $0.33\,L_{\odot}$, and a mass of $0.46\,M_{\odot}$, located in the Lupus I cloud, approximately 155 pc away from Earth. Its disk spectrum shows detections of $^{12}CO_2$, $^{13}CO_2$, H_2O, HCN, C_2H_2, and OH [16].

The authors employ Local Thermal Equilibrium (LTE) slab models to determine the temperature, column density, and emitting radius of the species under investigation. These parameters are obtained through χ^2-fitting of Gaussian line profiles. The models explore a parameter grid with column densities ranging from 10^{14} to $10^{22}\,\text{cm}^{-2}$ in logarithmic steps of 0.166, temperatures spanning from 100 to 1500 K in 25 K increments, and emitting radii varying from 0.01 to 10 AU in logarithmic steps of 0.03. To minimize contamination from other species, spectral windows are applied, where only a small wavelength range is used for each fit.

An iterative procedure refines the measurements: once an estimate for a species is obtained, its contri-

bution is subtracted, and the process repeats until no further detections can be made. The final results are summarized in Table 1.

Molecule	Column density (cm^{-2})	Temperature (K)	Emitting radius (AU)
$^{12}CO_2$	2.2×10^{18}	400	0.11
$^{13}CO_2$	1.0×10^{17}	325	0.11
C_2H_2	4.6×10^{17}	500	0.05
HCN	4.6×10^{17}	875	0.06
H_2O	3.2×10^{18}	625	0.15
OH	1.0×10^{18}	1075	0.06

Table 1: Best estimates for column density, temperature, and emitting radius for the molecules in the disk around GW Lup. Data obtained using an LTE slab model grid and χ^2 fitting assuming Gaussian line profiles, adapted from [16].

2.3 Emission lines

Emission lines occur due to the energy transitions of molecules. During these transitions, photons are emitted at wavelengths corresponding to the energy differences between the two states, given by the relation:

$$E = \frac{hc}{\lambda}, \tag{1}$$

where E is the energy difference, h is the Planck constant, c is the speed of light in a vacuum, and λ is the emitted wavelength [17].
Molecules can undergo energy transitions through their three primary degrees of freedom: rotation, vibration, and bending. These transitions result in emission lines spanning the near-infrared (near-IR) to millimeter wavelengths. Although molecules also exhibit electronic transitions, these require higher energy levels and result in lines in the ultraviolet (UV) range, which lies outside the scope of this thesis [2].

2.3.1 Ro-vibrational lines

Vibrational transitions generally require higher energy than rotational transitions, and thus purely vibrational emission lines are rarely observed. Instead, **ro-vibrational transitions**—which combine both vibrational and rotational energy changes—are commonly detected. Each vibrational transition is associated with multiple rotational energy levels, described by changes in the rotational quantum number J.
For a symmetric molecule such as sulfur dioxide (SO_2), there are three fundamental vibrational modes:

1. The symmetric stretch (ν_1),
2. The asymmetric stretch (ν_3),
3. The bending or scissoring mode (ν_2),

as described in [2, 18]. These vibrational modes produce complex spectra characterized by overlapping rotational substructures within each vibrational band.
For linear molecules like SO_2, the vibrational behavior can be approximated by a harmonic oscillator, neglecting anharmonicity. Anharmonicity refers to the deviation from harmonic behavior, occurring when the restoring force is no longer proportional to displacement [19]. Under the harmonic oscillator approximation, the energy of a vibrational mode is:

$$E_v = h\nu\left(v+\frac{1}{2}\right), \tag{2}$$

where E_v is the energy of the vibrational mode, ν is the vibration frequency, v is the vibrational quantum number (an integer ≥ 0), and h is the Planck constant. The vibrational frequency ν is given by:

$$\nu = \frac{1}{2\pi}\sqrt{\frac{k}{\mu}}, \tag{3}$$

where k is the force constant of the bond, and μ is the reduced mass of the molecule [18].
Rotational transitions can be modeled as those of a rigid rotor, neglecting centrifugal distortion effects. The rotational energy levels are quantized as:

$$E_r = \frac{h^2}{8\pi^2 I}J(J+1), \tag{4}$$

where E_r is the rotational energy, J is the rotational quantum number (an integer ≥ 0), and I is the moment of inertia, defined as $I = \mu r^2$, where r is the bond length [18].
The total energy for a ro-vibrational transition is the sum of the vibrational and rotational contributions:

$$E_{rv} = E_v + E_r = h\nu\left(v+\frac{1}{2}\right) + \frac{h^2}{8\pi^2\mu r^2}J(J+1). \tag{5}$$

The HITRAN database [20] provides line data for various molecules, including ro-vibrational transitions, as illustrated in Figures 6 and 5.

2.3.2 Line broadening

Emission lines observed in real-world spectra are broadened by three primary mechanisms:

1. Natural broadening: A consequence of the uncertainty principle, particularly prominent in transitions involving excited states with short lifetimes.

2. Pressure broadening: Caused by molecular collisions in a gas, which perturb energy levels.

3. Thermal (Doppler) broadening: Due to the relative motion of molecules, resulting in slight Doppler shifts in wavelength [2].

When Doppler and turbulent broadening dominate, the emission line profile can be approximated by a Gaussian:

$$\phi_\nu = \frac{1}{\Delta\nu_D\sqrt{\pi}}\exp\left[-\left(\frac{\nu-\nu_{12}}{\Delta\nu_D}\right)^2\right], \tag{6}$$

where ν_{12} is the central frequency of the line, $\Delta\nu_D$ is the Doppler width, which depends on the gas temperature T_{gas} and the turbulent velocity v_{turb} [21].

2.3.3 Optical depth effects

The intensity of emitted photons depends on the number of molecules along the line of sight. As molecular column density increases, photon absorption by the medium (self-absorption) becomes significant, reducing the escape fraction. This effect is quantified by the optical depth τ. For N molecules per cm^{-2}, the optical depth for a transition is:

$$\tau_{12} = \frac{N\lambda_{12}^2 A_{12}}{8\pi}\left(\frac{g_1}{g_2}p_2 - p_1\right), \tag{7}$$

where λ_{12} is the transition wavelength, A_{12} is the Einstein coefficient for spontaneous emission, g_1 and g_2 are statistical weights, and p_1 and p_2 are level populations.
At a frequency ν, the optical depth profile is given by:

$$\tau_\nu = \frac{\tau_{12}}{\Delta\nu_D\sqrt{\pi}}\exp\left[-\left(\frac{\nu-\nu_{12}}{\Delta\nu_D}\right)^2\right]. \tag{8}$$

The radiative transfer equation, $\frac{dI_\nu}{ds} = j_\nu - \kappa_\nu I_\nu$, relates the intensity I_ν, path length s, emission coefficient j_ν, and absorption coefficient κ_ν. Integrating this equation yields the total line intensity:

$$I = B_{\nu_{12}}(T)\int\left(1-e^{-\tau_\nu}\right)d\nu, \tag{9}$$

where $B_{\nu_{12}}(T)$ is the Planck function at temperature T.

2.4 Why SO_2

Understanding sulfur depletion in protoplanetary disks requires the identification of molecules that can effectively trace sulfur abundance. As previously mentioned, ALMA observations have detected only two sulfur-bearing species in the disk of DM Tau: carbon monosulfide (CS) and sulfur dioxide (SO_2) [5]. Of these, SO_2 is particularly well-suited for this study due to its extensive and detectable ro-vibrational spectrum within the observation range of the James Webb Space Telescope (JWST) Mid-Infrared Instrument (MIRI).
We used molecular data from the HITRAN Online database [20] for the most abundant isotope of SO_2 (94% abundance). All lines within the JWST MIRI observing range were selected, and the resulting spectrum is shown in Figure 5. This figure highlights two regions of high-intensity emission lines: from 5 to 10 μm and from 15 to 25 μm. These regions correspond to distinct ro-vibrational bands of SO_2, as described below:
- 5-10 μm range: This region includes strong ro-vibrational bands arising from transitions within asymmetric stretch (ν_3) and bending (ν_2) vibrational modes. These modes produce dense clusters of emission lines with high intensities, making them prominent and easier to distinguish from the background.
- 15-25 μm range: In this region, ro-vibrational transitions primarily involve the bending (ν_2) vibrational mode. The lines are more widely spaced compared to the 5-10 μm range, which reduces blending and enhances their distinguishability despite their somewhat lower intensities.
Outside these regions, the spectral intensity remains relatively low, forming a continuum. The dense clustering of lines in the 5–10 μm range and the well-separated lines in the 15-25 μm range provide complementary advantages for sulfur detection in protoplanetary disks.

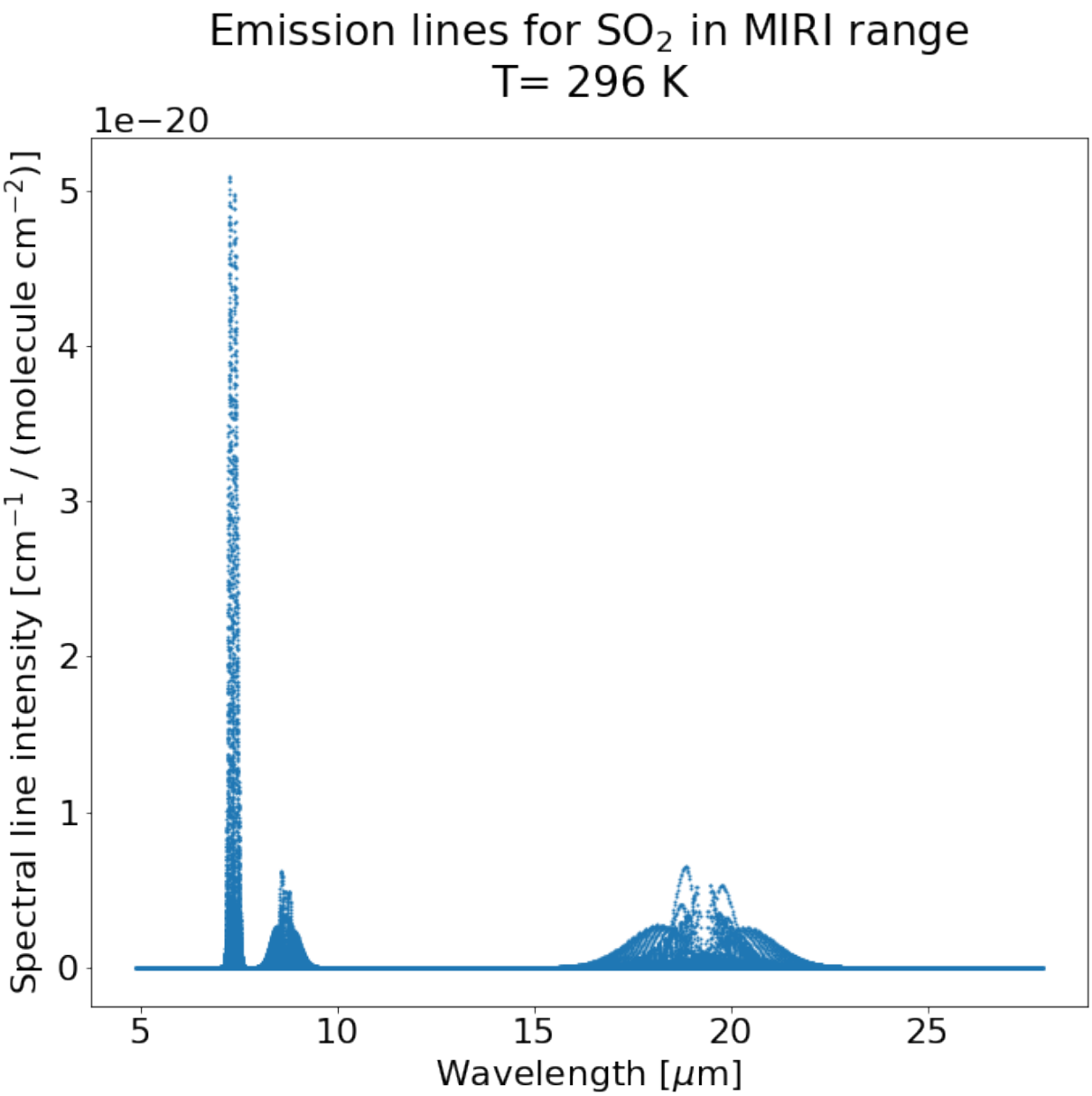

Figure 5: Emission lines of the most abundant SO_2 isotope, based on data from the HITRAN Online database [20]. The x-axis shows the wavelength in μm, and the y-axis represents the intensity for a single molecule per unit volume. Each point represents the peak of an emission line. Note that line broadening effects are not included in this figure. A total of 345,642 emission lines are shown.

In contrast, the spectrum of CS (Figure 6) contains significantly fewer emission lines within the JWST MIRI wavelength range. Although the peak intensity of CS emission lines is higher than that of SO_2, the limited number of lines makes it less favorable as a sulfur tracer. Given the expected similar column densities of CS and SO_2, CS lines are more likely to be masked by overlapping spectral features from other species.
Therefore, SO_2 is the more advantageous choice as a tracer for sulfur detection, combining a dense and distinguishable line spectrum with favorable coverage in the JWST MIRI range.

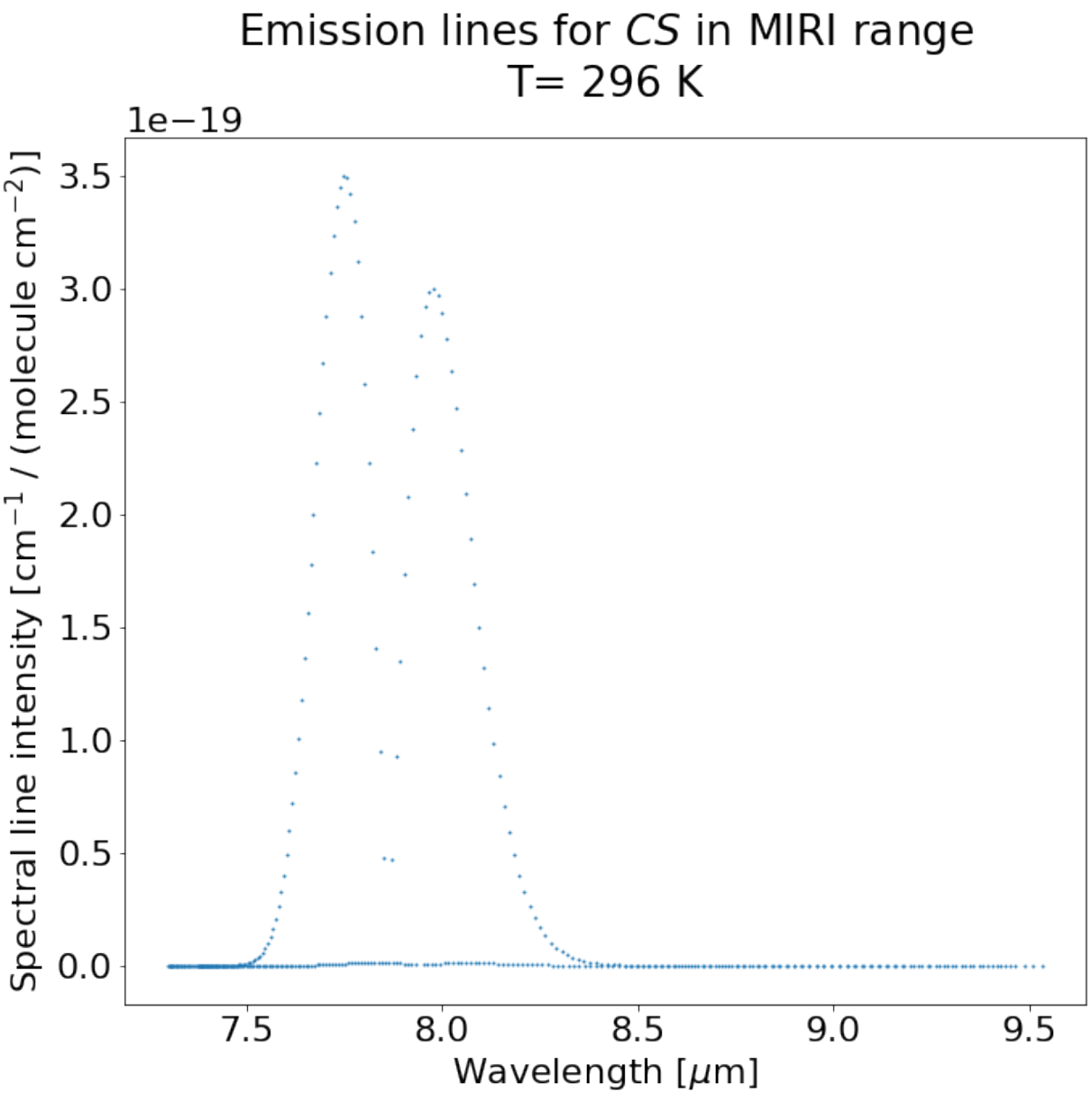

Figure 6: Emission lines of CS in the JWST MIRI MRS wavelength range, based on data from [20].

2.5 Radiative Transfer and ProDiMoPy

ProDiMo is a versatile modeling code designed for studying protoplanetary disks [22]. Its reliability has been demonstrated in applications such as modeling a typical T Tauri star's disk and a molecular cloud with properties resembling TMC-1, the Taurus Molecular Cloud, a region known to be a nursery for protoplanetary disks [2]. T Tauri stars themselves are young stars similar in mass to the Sun, making them ideal for exploring early disk chemistry.

The Python implementation, ProDiMoPy, allows for the generation of simplified models, including 0D slab models. These models assume uniform properties across the slab, providing an efficient way to study radiative transfer and molecular line emission. Key input parameters for such a model include the gas column density of the molecule under consideration, the gas temperature, turbulent velocity,

molecular mass, isotopic ratios, and the wavelength range for computation. Additionally, line data, including molecular transitions, statistical weights, and energy levels, is retrieved from the HITRAN database [20].
In ProDiMoPy, line broadening is a crucial aspect that accounts for the combined effects of turbulence and thermal motion within the gas. The broadening velocity, v_g, combines these contributions and is expressed as:

$$v_g = \sqrt{v_{\text{turb}}^2 + \frac{2k_B T_g}{m_{\text{mol}}}}, \tag{10}$$

where v_{turb} is the turbulent velocity, T_g is the gas temperature, and m_{mol} is the molecular mass.
The level populations of the molecule are determined using the Boltzmann distribution, which describes the ratio between the populations of two energy levels based on their energies, degeneracies, and the gas temperature:

$$\frac{p_u}{p_l} = \frac{g_u}{g_l} \exp - \frac{E_u - E_l}{k_B T_g}, \tag{11}$$

where E_u and E_l are the energies of the upper and lower levels, respectively, and g_u and g_l are their degeneracies. These populations are normalized across all possible energy levels using the partition function, $Q(T_g)$, a temperature-dependent quantity precomputed from HITRAN data.
The interaction of radiation with the slab is characterized by the optical depth τ_ν, which quantifies the absorption at a given frequency ν:

$$\tau_\nu = \frac{A_{ul}}{8\pi^{3/2}} \frac{c^3}{\nu_{12}^3} \frac{N_g}{v_g} \left(\frac{g_u}{g_l} p_l - p_u \right). \tag{12}$$

Here, A_{ul} is the Einstein coefficient for spontaneous emission, ν_{12} is the frequency of the transition, and N_g is the gas column density.
Radiative transfer is then computed using the intensity of emitted radiation at a given frequency, I_ν. This is derived from the radiative transfer equation, assuming blackbody radiation from the source, and is given by:

$$I_\nu = B_\nu(T_g) \left(1 - e^{-\tau_\nu}\right), \tag{13}$$

where $B_\nu(T_g)$ represents the Planck function for a gas at temperature T_g:

$$B_\nu(T_g) = \frac{2h\nu^3}{c^2} \frac{1}{e^{h\nu/k_B T_g} - 1}. \tag{14}$$

This framework enables ProDiMoPy to produce synthetic spectra by summing the contributions of individual lines over the specified wavelength range. The resulting spectra reflect the physical conditions of the gas and the specific molecular transitions involved.
By utilizing the uniform conditions of the 0D slab, ProDiMoPy provides a computationally efficient yet accurate means to study molecular line emission and the underlying radiative transfer processes. These models offer valuable insights into the physical and chemical properties of molecular gas in protoplanetary environments.

2.6 JWST MIRI MRS data

The MRS instrument has four different channels, each observing in different wavelength ranges. Each channel consists of three bands and can observe one band at a time. The flight-measured properties for each of these channels is given in table 2 [7].

FOV name λ-range (μm)	FOV (arcsec)	Number of slices	Sub-band name	λ-range (μm)	Resolving power ($\lambda/\Delta\lambda$)
Channel 1 4.9–7.65	3.2 × 3.7	21	***SHORT (A)***	4.90–5.74	3,320–3,710
			MEDIUM (B)	5.66–6.63	3,190–3,750
			LONG (C)	6.53–7.65	3,100–3,610
Channel 2 7.51–11.7	4.0 × 4.8	17	***SHORT (A)***	7.51–8.77	2,990–3,110
			MEDIUM (B)	8.67–10.13	2,750–3,170
			LONG (C)	10.01–11.70	2,860–3,300
Channel 3 11.55–17.98	5.2 × 6.2	16	***SHORT (A)***	11.55–13.47	2,530–2,880
			MEDIUM (B)	13.34–15.57	1,790–2,640
			LONG (C)	15.41–17.98	1,980–2,790
Channel 4 17.7–27.9	6.6 × 7.7	12	***SHORT (A)***	17.70–20.95	1,460–1,930
			MEDIUM (B)	20.69–24.48	1,680–1,770
			LONG (C)	24.40–27.90	1,330–1,630

Table 2: Properties of each channel used for medium-resolution spectroscopy using MIRI. Table from [7]

2.6.1 Preprocessing JWST data

The raw data obtained from JWST undergoes a data reduction routine outside the scope of this thesis. The data reduction for the spectrum of the disk around GW Lup is described in [16] and used throughout this thesis. The reduced data provides a spectrum stitched together containing data from all the channels. Subtracting the continuum results in a spectrum showing only the emission lines of an actual observation, which is comparable to the mock spectra obtained from ProDiMoPy. An example of this can be seen in figure 7, which is the T Tauri star disk around GW Lup[21].

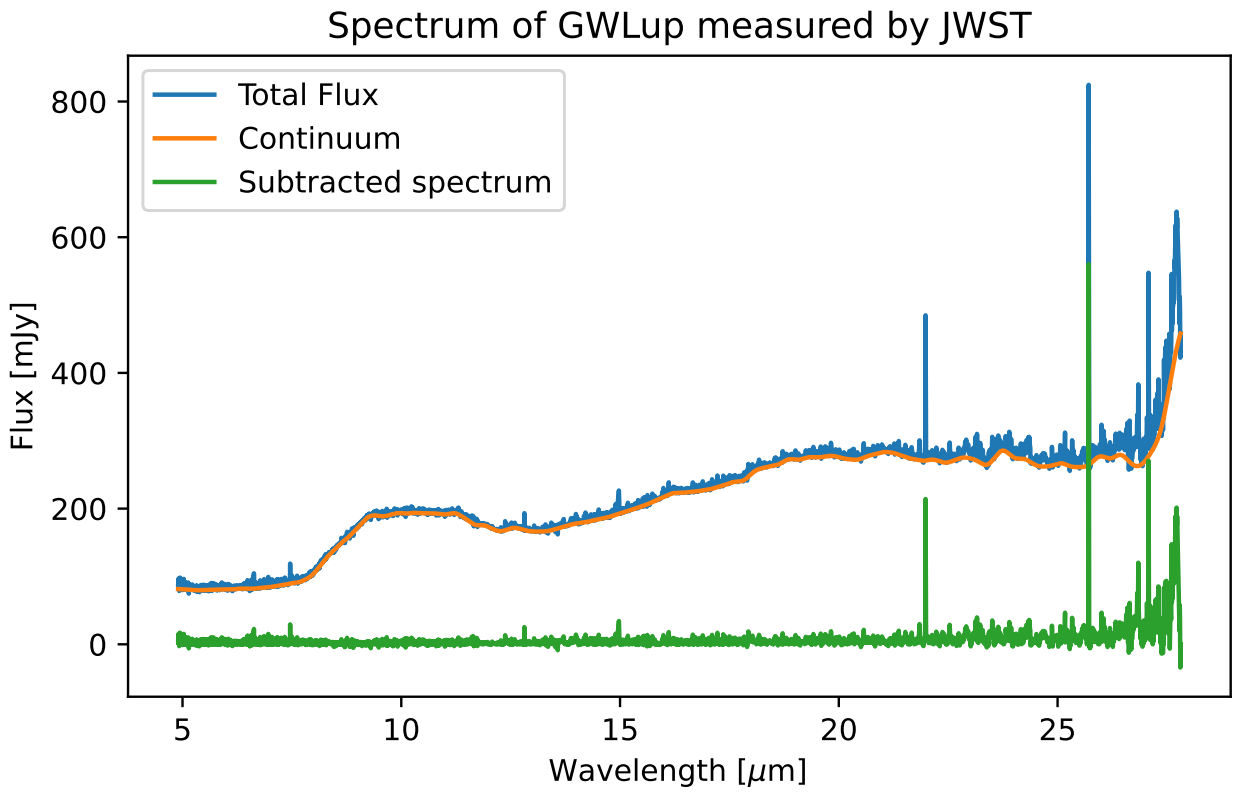

Figure 7: Full spectrum of the disk around GWLup, with lines showing the full spectrum, the continuum, and the continuum subtracted line emission spectrum. Data obtained from [21].

Noise originates for example from, detector gain variations, thus pixel-to-pixel gain variations, typically up to a couple percent. These are usually calibrated for using a detector flat-field. There are also intra-pixel gain variations, which is the variation in gain within a pixel itself. This is due to pixel responsivity or quantum efficiency within the pixel area. There are methods for mitigating this effect, which makes JWST less affected than previous IR missions by this effect. The way JWST pixels are read also generates noise, mostly called the $1/f$ noise, which has a stochastic nature, meaning each frame will have its own unique signature. Part of this effect can be removed by using reference pixels, but some fraction will always remain. It is also noteworthy that the mid infrared range is less affected by this effect than the near infrared observations when using the MIRI instrument. There is also persistence, which is a sort of memory effect, resulting in an afterglow that decays over time. There are several other noise sources within an observation, some of them can be accounted for, but there will always be a resulting noise level [23]. To be able to test and evaluate the methods developed in this thesis, we require to have a realistic realisation of the instrument noise. For this, the debris disk spectrum HD172555 is used. This spectrum is known to contain no molecular emission and atomic emission lines will be masked out. This leaves continuum emission with a realistic noise profile.

3 Methods

3.1 Slab models

ProdimoPy is used to generate LTE slab models of various species. This means we do not consider any gradient in temperature throughout the entire disk. This is quite common for 1D slab models [14]. Our main variables are temperature and column density. We consider for simplicity only the most abundant isotope, which is about 94% for SO_2 [20]. The width parameter or turbulent velocity is kept constant for all models we consider in this thesis, with its value kept at 2.0 km s^{-1}. The partition sums used for calculating the energy level populations are precomputed and We then use the HITRAN database [20] to get the emission lines of the given isotopes for the molecule in a given wavelength range. This data includes the quantum numbers characterizing the transition, as well as the expected line intensity. This module encapsulates line broadening and determines the total line intensity using equation 9.

3.1.1 Convolving to MIRI MRS resolution and sampling

To compare the generated slab models with the JWST data, the models must be convolved to match the resolving power of the MIRI MRS, as shown in Table 2. This process relies on the resolving power and the upper and lower wavelength bounds for each channel. Since these values are not fixed, we have incorporated several options within the framework to define the resolving power. The choices include using the average of the upper and lower bounds, selecting the maximum value, or using the minimum value for the resolving power within the channel.
Additionally, to handle wavelength overlap between adjacent channels, I investigated four distinct methods: (i) setting the upper bound of the lower channel as the lower bound for the next channel, (ii) taking the lower bound of the higher channel as the upper bound for the lower channel, (iii) using the maximum wavelength range for the channel with the highest resolving power, and (iv) using the maximum wavelength range for the channel with the lowest resolving power. These options are applied separately for the short, medium, and long wavelength channels, as detailed in Table 2. The different settings and the corresponding resolutions per channel in the convolved spectrum are visualized in Figure 8. This figure thus shows to which the small overlapping wavelength ranges are attributed and assigns a single value for the resolving power to each channel. This way, each wavelength value will correspond to only one channel and each channel has one fixed resolving power, which allows us to convolve the spectrum to match MIRI MRS.

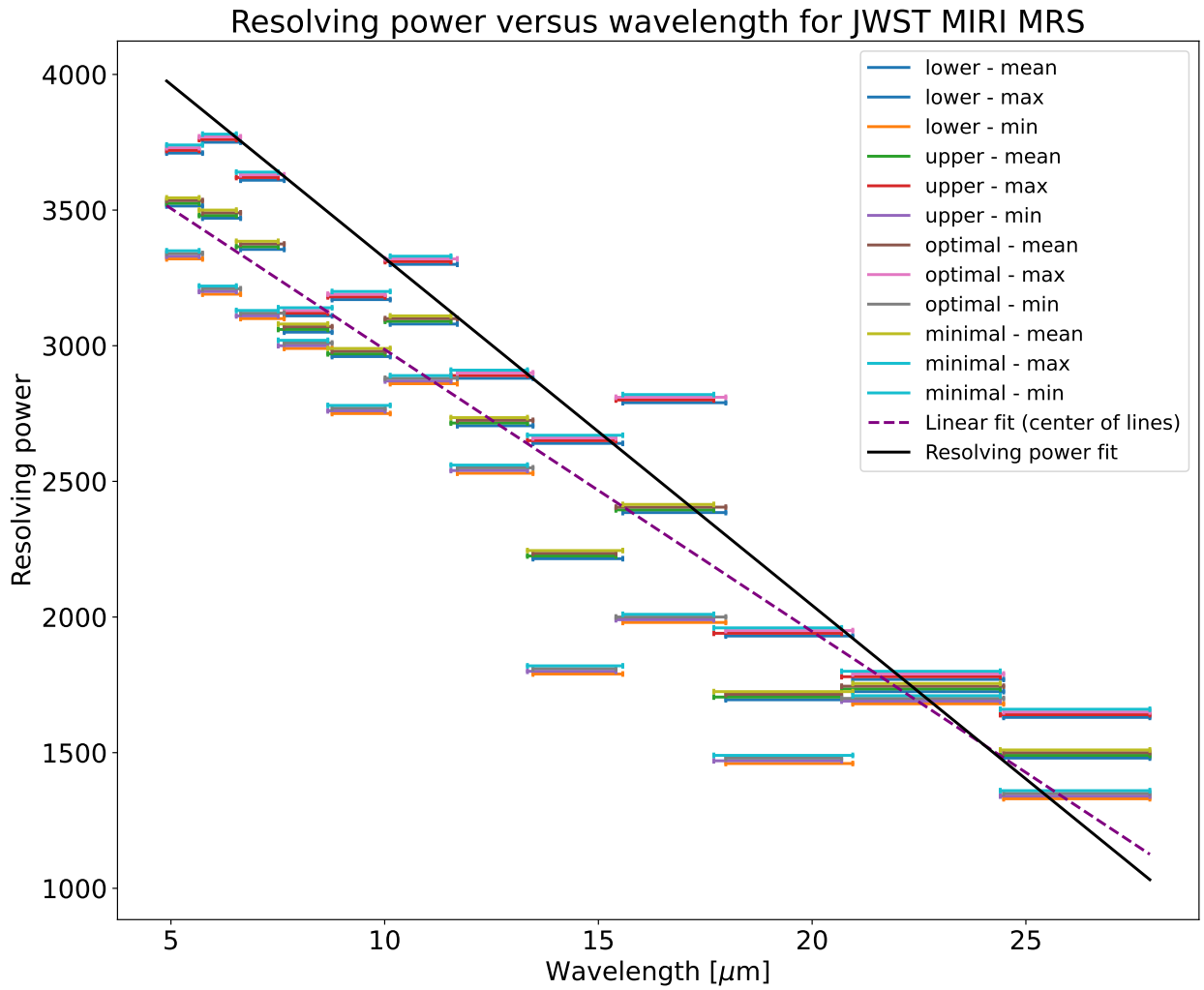

Figure 8: Varying settings of the convolver, showing options for choosing a resolving power and removing wavelength overlap. The continuous line shows an approximate functional fit of the resolving power from [24]. The dashed line shows a linear fit through the center of each of the marked lines.

A functional fit for the resolving power is given by $R(\lambda) = 4603 - 128\lambda(\mu\text{m}) + 10^{-7.4\lambda(\mu\text{m})}$ [24], which is also shown in Figure 8. This fit closely matches the resolving power settings used in our implementation, though with notable differences, which is especially apparent if we compare the linear fit through the channel centers. For this work, we use the channel-specific resolving power provided in Table 2 to maintain consistency and accuracy in model generation. The minimum is mostly used to represent a worst-case scenario, so we can expect real observations to have at least equal sampling of the wavelength range.

The convolving process results in a list of frequencies in GHz, with corresponding specific intensities in erg s^{-1} cm^{-2} sr^{-1} Hz^{-1}. To convert these frequencies into wavelengths in microns, we use the relation:

$$\lambda\,[\mu\text{m}] = \frac{c}{\nu\,[\text{GHz}] \times 10^{-3}}. \tag{15}$$

The specific intensity is then converted into mJy by multiplying by 10^{26} and the solid angle $\Delta\Omega$,

which is defined as:

$$\Delta\Omega \equiv \frac{\text{emitting area}}{\text{distance}^2} = \frac{\pi R^2}{d^2}, \tag{16}$$

where R is the radius of the emitting region (assumed circular on the sky), and d is the distance from the observer to the source. While R is often unknown and d varies depending on the observation, the normalization of both models and observations effectively balances out these uncertainties, allowing for meaningful comparisons.
Once the convolving process is complete, the model loops over each molecule in the spectrum, adjusting the data for each channel based on the wavelength bounds determined earlier. For each channel, the relevant molecular data is extracted and convolved according to the selected settings. After the data from all channels is convolved, it is concatenated, resulting in a complete spectrum for each molecule across the MIRI MRS wavelength range. This process is repeated for each molecule included in the model. Finally, all of the individual spectra are summed to produce the total modeled emission spectrum. This ensures that the generated slab models are compatible with the JWST observations, allowing for a direct comparison between the two.

3.2 Generating a noise model

The spectrum of a debris disk, which is characterized by the absence of molecular emission lines but exhibits the typical noise profile observed in JWST MIRI data [25], serves as a baseline for the analysis. To simulate the presence of molecular emission, such as SO_2, simulated slab spectra are overlaid on the debris disk spectrum. These simulated slab spectra are normalized to 1 and then scaled by a factor, denoted as k, which is defined as:

$$k = \text{SNR} \times \sigma_{\text{noise}}, \tag{17}$$

where SNR represents the desired signal-to-noise ratio (in terms of standard deviations) for the simulated peaks, and σ_{noise} is the standard deviation of the noise in the original debris disk spectrum.
Prior to the addition of the simulated molecular emission, the continuum of the debris disk spectrum is removed using a simple moving average with a window size of 100 data points. This method, while effective in continuum subtraction, introduces edge effects at the boundaries of the spectrum, which are discarded to preserve the integrity of the data. To ensure that the residual noise profile remains consistent with observational characteristics, the moving average is shifted downward before subtraction based on the median of the differences between the continuum and the spectrum. This ensures the noise profile introduces no bias [25]. Furthermore, any peaks in the debris spectrum that exceed a defined signal-to-noise threshold are capped to prevent unrealistic signal enhancements before the molecular spectra are incorporated. The continuum is shown in figure 9. An example of a capped spectrum with SO_2 added in will be shown later in figure 10.

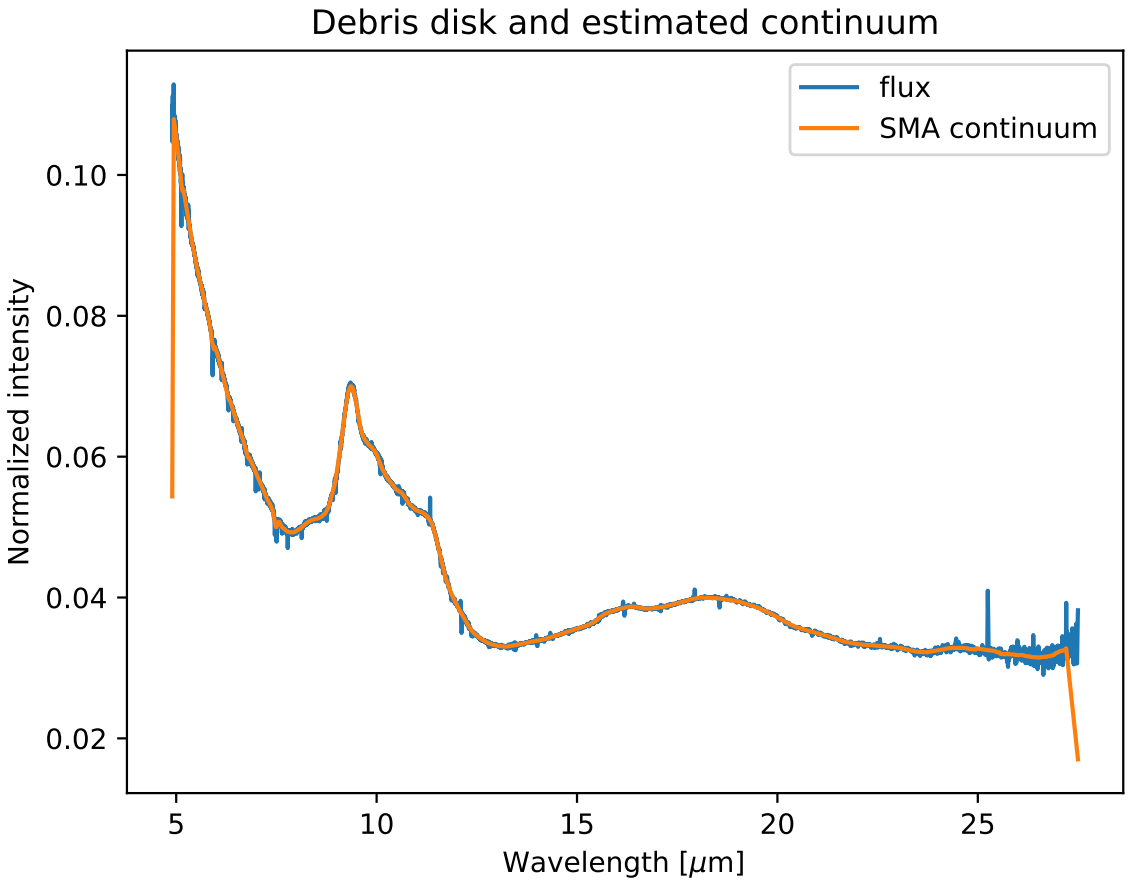

Figure 9: Debris disk spectrum with the continuum highlighted. The continuum is computed using a simple moving average with a window size of 100, accounting for the broad features in the noise. Edge effects caused by the moving average are evident near the spectrum boundaries.

3.3 Cross correlation technique

3.3.1 Detecting the presence of SO_2 using cross-correlation

We are dealing with spectra that must be normalized since we do not know every detail of the object and want to correlate the slab models with actual observations. If we want a quantitative measurement of abundance, we need to scale with the emitting area to match the slab models with the actual observations, which is too complicated to be a first step. Better would be to see if we can detect the presence of SO_2 without any quantitative measurement, for which we can use normalized spectra. There is also the possibility that this leads to a first temperature estimate of the SO_2. To detect SO_2, we want to estimate the best-fitting slab model and overlay it to see if the peaks in the spectrum match up.
The best-correlating spectrum is determined via cross-correlation by computing the Pearson Correlation Coefficient (r) between the observed spectrum and a grid of normalized SO_2-only slab model spectra with varying temperatures and column densities. The coefficient r is given by

$$r = \frac{\sum(x-m_x)(y-m_y)}{\sqrt{\sum(x-m_x)^2\sum(y-m_y)^2}}, \tag{18}$$

where x represents the intensity values of the observed spectrum at each wavelength, y represents the intensity values of the slab model spectrum at the corresponding wavelengths, and m_x and m_y are the mean intensity values of x and y, respectively. This metric quantifies the similarity between the observed and model spectra, allowing identification of the best-correlating slab model parameters. This returns a cross-correlation coefficient and a p-value. This p-value denotes the statistical significance, thus the effect of randomness on the cross-correlations, where a low p-value suggests the correlation to be unlikely caused by noise, thus indicating SO_2 presence. In other words, the p-value is a measurement of the probability of an uncorrelated dataset to produce a similar correlation coefficient [26]. This means the correlation coefficient is affected by the relative peak heights. The dataset used for cross-correlation consists of SO_2 column densities in units of cm^{-2} varying between 1 and 17.5 in step sizes of half integers in $\log_{10}$ base. The temperature varies between 100 and 1100 K in step sizes of a hundred Kelvin.
To analyze how well the method performs, we will add SO_2 at a given temperature and column density to the debris disk given a predefined signal-to-noise ratio. We will investigate whether we can retrieve the SO_2 using the cross-correlation method described above. An example of such a spectrum of SO_2 with the debris disk is shown in figure 10. We exclude models with column densities below 10^4 cm^{-2}, as those mock spectra do not contain any signal.

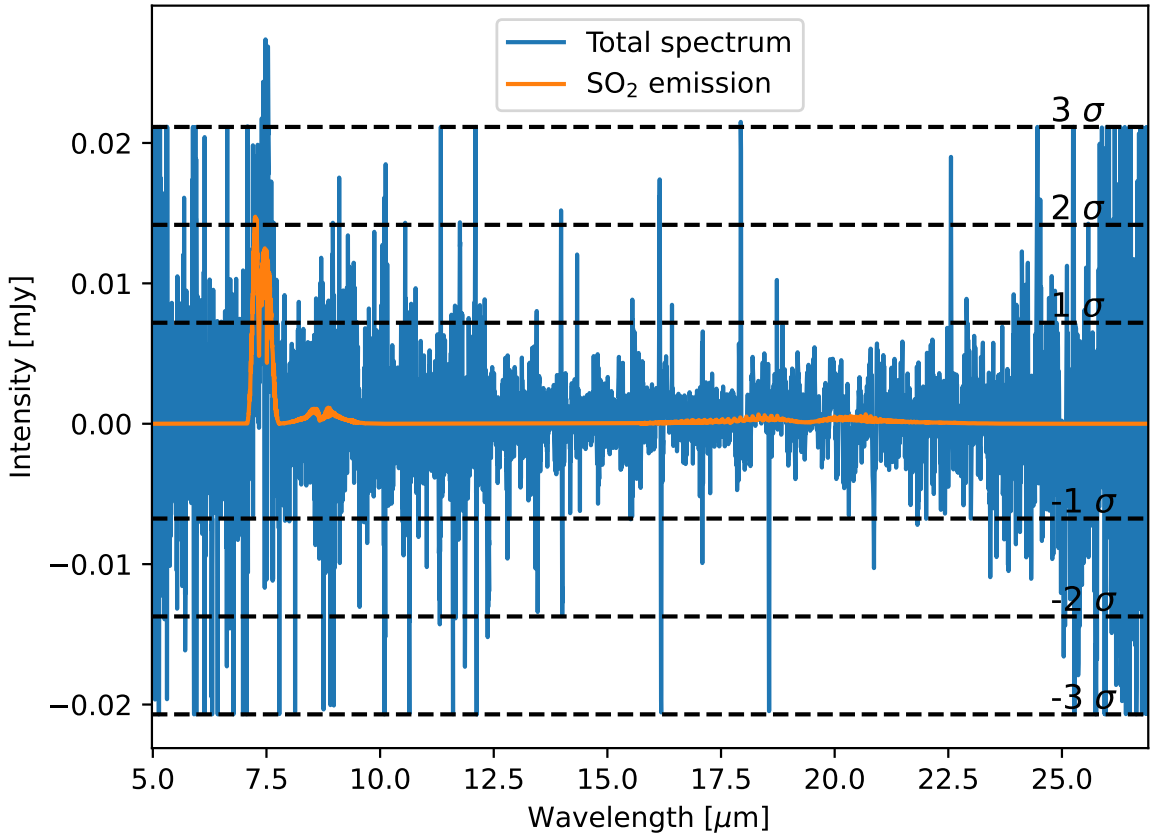

Figure 10: Mock spectrum using a slab model with SO_2 at a temperature of 900K and a column density of 10^{14} cm^{-2}, added at a signal-to-noise ratio of 3 to the debris disk spectrum.

For this spectrum, the correlation matrix with the aforementioned grid of mock spectra with accompa-

nying p-values is computed. This matrix is shown in figure 11. We observe an outlier at a temperature of 100K and a column density of $10^{4.5}$, which needs to be investigated further as to the origin of this phenomenon, as we observe it quite often. We call it an outlier as it has a reasonably consistent correlation regardless of the input, and has seemingly no relation to the other values in the grid. At a signal-to-noise of 3 it is almost always the best correlating mock spectrum for the chosen grid, where we define the best match as the mock spectrum with the highest correlation coefficient while having a corresponding p-value below a threshold, which is arbitrarily chosen to be 0.05. When moving to a signal-to-noise of 6, this phenomenon occurs less frequent, but still is there. We do see that often the second best correlating mock spectrum has parameters that are far closer to the actual values of the parameters of the slab model used, a fact that we will use when trying to calibrate the result to maximize performance in estimating the temperature and column density in an observation. If we solely look at the best-correlating slab model and the actual model with debris disk, we get for each signal-to-noise value a grid such as in figure 12, where the result for a mock spectrum with SO_2 at a signal-to-noise ratio of 3 is shown.

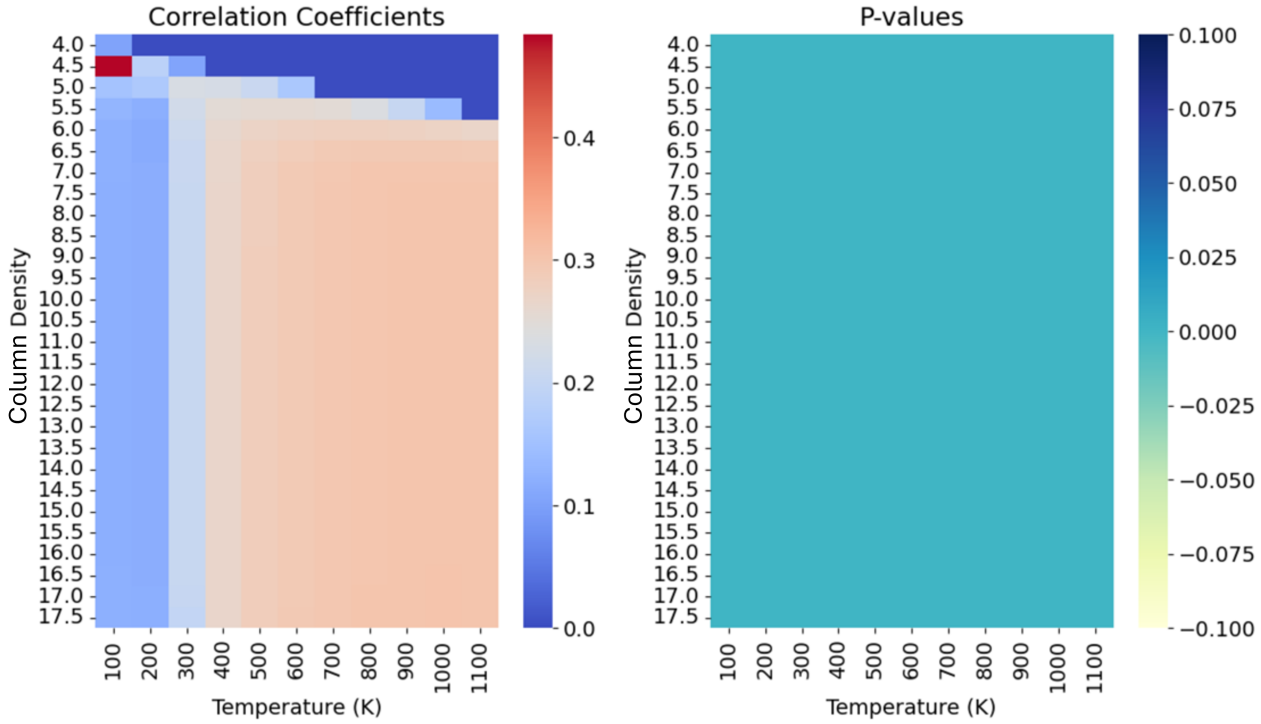

Figure 11: Cross-correlations with the SO_2 slab model grid for a mock spectrum at a temperature of 900K and a column density of 10^{14} cm^{-2}, added at a signal-to-noise ratio of 3.

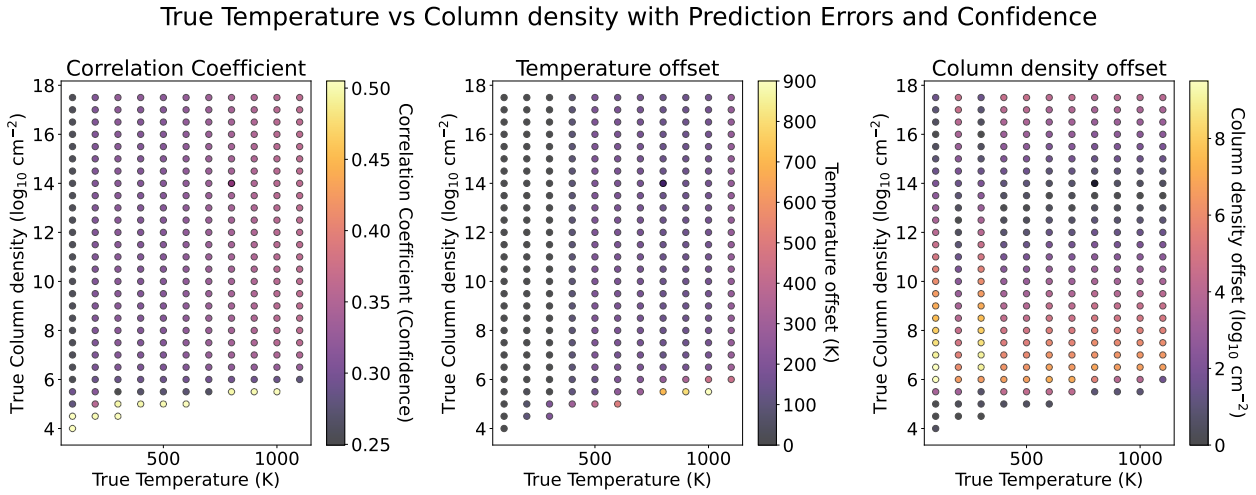

Figure 12: Visualization of the behavior of the best estimations for different true values corresponding to the used slab models at signal-to-noise of 3. The first subplot shows the correlation coefficient we got at that point, the second the difference in temperature between the true slab model and the highest correlating fit, the third the difference in column density for the true spectrum and best correlating fit.

3.3.2 Calibrating predictions

To investigate whether our predictions of temperature and column density from cross-correlation with simulated spectra can be improved, we aim to estimate the true values while accounting for systematic offsets in different regions of the parameter space. This approach is essential because initial predictions from cross-correlation can exhibit consistent biases depending on the local structure of the parameter space and the density of available spectra with which we correlate, as this is a discrete grid in practice. Each such a spectrum is a point in the grid, which we will refer to as training points. To address this, we developed a method that calculates a weighted average of the top cross-correlation matches while excluding outliers, thereby providing more accurate and robust estimates of temperature, column density, and their associated uncertainties.

We begin by identifying the five best-correlating slab model spectra for a given observation. For each parameter (temperature and column density), we calculate a weighted average, where the weights are proportional to the cross-correlation coefficients of the matches. Outliers are excluded based on user-defined thresholds to mitigate the influence of aberrant matches. For instance, anomalous matches such as (100 K, $10^{4.5}$ cm^{-2}) can be excluded if the majority of other matches suggest significantly different values. The weighted averages yield preliminary predictions of temperature, column density, and correlation coefficients. These predictions form the basis for further refinement.

To estimate the true values and their uncertainties, we leverage the systematic behavior of cross-correlation offsets across the parameter space, visualized in Figure 12. We calculate the Euclidean distance between our predictions and all known training points, selecting the k-nearest neighbors (where k is a user-defined parameter). A weighted average of the k-nearest neighbors is then computed, incorporating both the distances and their respective cross-correlation coefficients as weights. Closer neighbors with higher correlation coefficients contribute more to the final estimate. This process ensures that predictions are informed by the local structure of the parameter space, improving accuracy in regions with consistent systematic offsets.

Uncertainty estimates are derived by applying the same methodology to the errors of the selected neighbors. These errors are defined as the difference between the predicted values (from cross-

correlation) and the true values in the set of training points. A minimum of three neighbors is required within the predicted uncertainty bounds. If fewer neighbors are found, the bounds are iteratively expanded until this condition is met. The final uncertainty is computed as a weighted average of the selected neighbors' errors. Using these neighbors, we also determine the minimal correlation coefficient, which serves as a confidence threshold for predictions in that part of the parameter space.
To evaluate the performance of this method, we compute the mean absolute error (MAE) and root-mean-square error (RMSE) for both temperature and column density predictions. A composite score is calculated by averaging the MAE and RMSE for each parameter, providing a singular performance metric for comparison. We optimize the choice of k by varying it and evaluating its impact on the performance metrics. For temperature estimation, the optimal value of k is found to be 19; for column density estimation, $k = 16$ is optimal. Considering overall performance, the best value is $k = 18$. For this k, we achieve a temperature MAE of 40.64, RMSE of 51.14, and correlation coefficient of 0.99, while for column density the corresponding values are 3.88, 4.61, and 0.36.
The results indicate that temperature predictions are highly reliable, as evidenced by the high correlation coefficient and low error values, with an average mismatch of approximately half a grid step. In contrast, column density predictions exhibit larger errors, with deviations spanning multiple grid steps and a lower correlation coefficient, suggesting greater uncertainty. This method is sensitive to the density of training points in the parameter space and depends on the signal-to-noise ratio (SNR) assumed for observations. As the SNR changes, the calibration of the method and resulting predictions may also vary. To investigate these effects, we apply the calibration method across the entire grid of spectra for different SNR values, visualized in Figure 13. For an SNR of 3, the calibration significantly reduces average errors, as shown in Figure 13. Similar improvements are observed for other SNR values. Additionally, Figures 14 and 16 illustrate how the performance evolves with varying SNR, showing strong fluctuations in temperature offsets at low SNR, while column density offsets remain relatively stable. However, the discrete nature of the model grid introduces limitations, as all slab models are sampled on the same grid, which differs from the true parameter space.

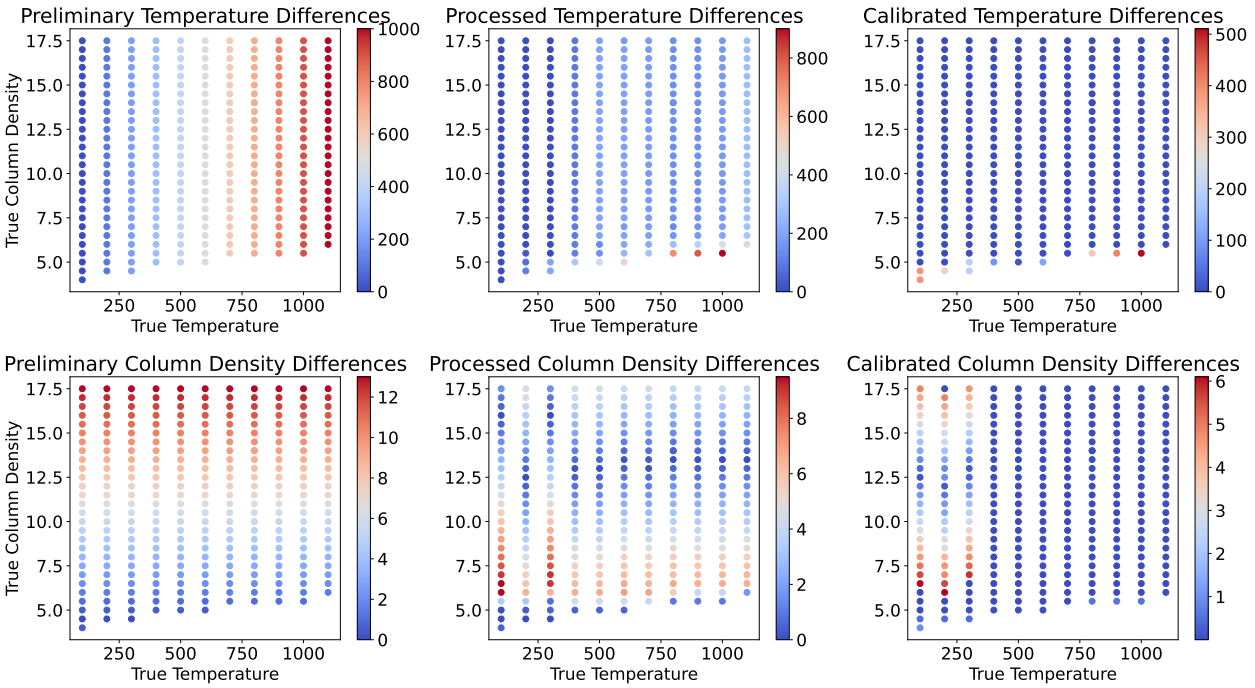

Figure 13: The impact of the calibration method on the parameter space with a signal-to-noise value of 3, where the first column of plots shows the results from always assuming the highest correlating model, the second from taking the weighted average while excluding outliers in the best matches, and the third the estimation of the true best values using the calibration method.

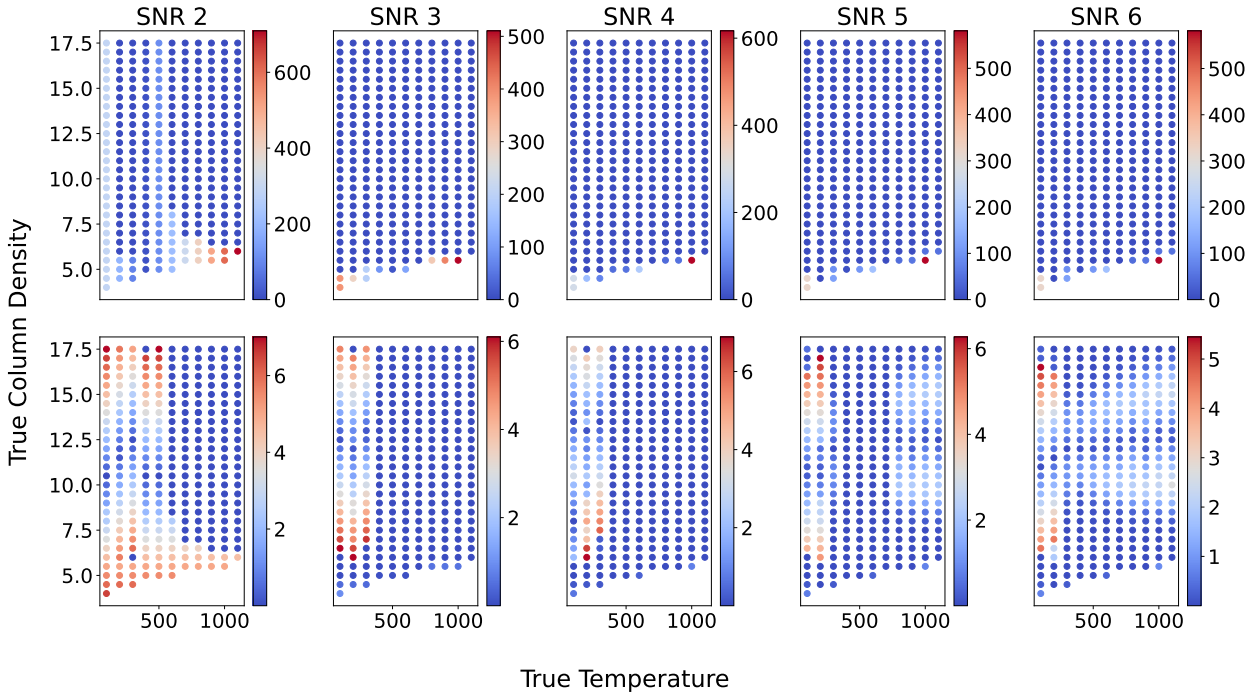

Figure 14: Impact of signal-to-noise ratios on the difference between predicted values and true values across the parameter space for the full calibration method. The top row shows the offsets in temperature and the bottom row in column density. Each subplot has the same values on the x and y-axis.

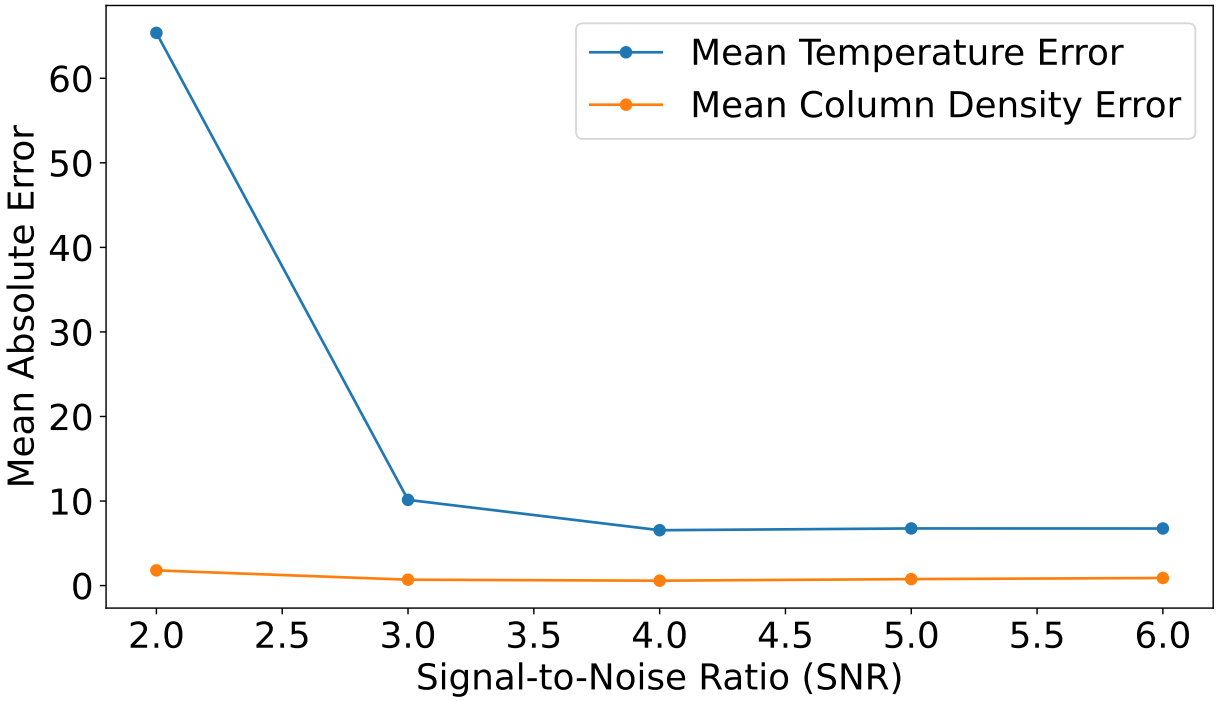

Figure 15: Impact of signal-to-noise ratios in mock spectra on the mean absolute error of the difference between predicted values and true values across the parameter space for the full calibration method.

3.3.3 Combining calibrations

To create a single calibration applicable across all signal-to-noise ratios (SNRs), we combine the individual calibrations for each SNR into a unified solution. Since the SNR for an actual observation is unknown beforehand, this approach ensures that the calibration remains generalizable.
The combined calibration is constructed as a weighted average across the available SNR-specific calibrations. The weights are defined as $w_i = \frac{1}{1+\mathrm{SNR}_i}$, where i indexes the calibrations. This weighting scheme gives higher priority to lower-SNR results, as they typically yield more reliable predictions.
This method is applied uniformly across all temperatures, column densities, and correlation coefficients throughout the parameter space. By integrating the results from all considered SNRs, we obtain a robust, single calibration that incorporates the strengths of each individual SNR-specific calibration while remaining adaptable to varying observational conditions.

3.4 Processing routines before applying cross-correlation

3.4.1 Preselecting spectral windows

To assess whether the accuracy of estimates derived from the cross-correlation method can be improved, we explore tailored preprocessing steps applied to the data. One such approach involves selecting spectral windows containing the main SO_2 emission bands. The SO_2 emission is generally confined to the spectral ranges between 7 and 9.5 microns and between 16 and 22 microns, as explained in section 2.4. This leads to four distinct strategies for evaluation: (i) focusing solely on the

first window, (ii) focusing only on the second window, (iii) considering both windows, and (iv) using the entire spectrum, as done in the previous analysis.
To evaluate the performance of these methods, we generate a calibration for each approach using the previously outlined procedures. Subsequently, the performance is tested on a separate set of mock spectra, which have not been taken into account in generating the calibration, and the accuracy of temperature and column density estimates is assessed once more. All evaluations are conducted while constraining the column density to values greater than 10^9 cm^{-2}, based on the observed behavior at lower column densities, where we see no signal below 10^5 and expect no observable signal below 10^{10}, as will be outlined in section 4.2.1. Due to computational limitations, the dataset used for calibration is sparse, and thus slightly less accurate. However, the results of the analysis should still provide meaningful comparisons across methods.
We observe that the performance varies across the parameter space The error in temperature estimation correlates with both temperature and column density, as shown in Figures 27 and 26. For instance, a higher temperature results in a larger error when using the second window, while the opposite is observed for the first window. These trends are consistent with the expected behavior as a function of varying temperature, where we see an increase in SO_2 emission in either band depending on temperature, as will be later outlined in section 4.2.1 in figure 26. Regarding column density, errors appear relatively constant across temperatures, with an increase in error at lower column densities. This behavior is consistent with our previous observations, where signal loss occurs at low column densities when the emitting area is kept constant.
In conclusion, using the full spectrum remains the most reliable method, as it minimizes outliers and provides the most consistent results across the parameter space. Additionally, it yields the lowest absolute error, making it the most robust approach for this analysis.

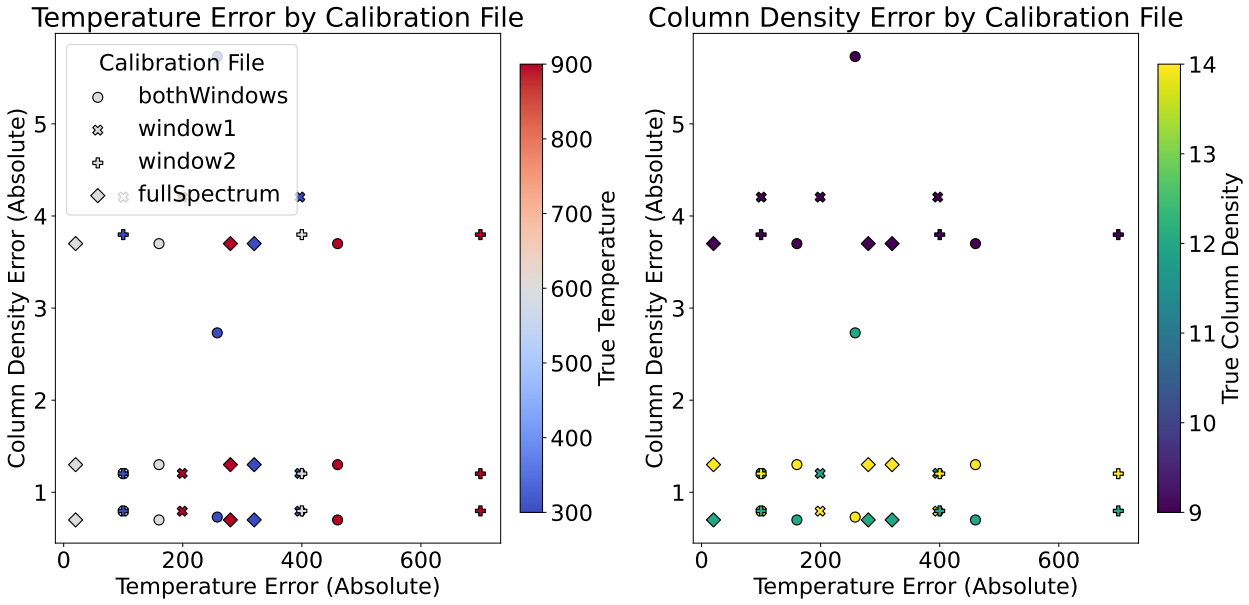

Figure 16: Temperature and column density prediction offsets for different spectral windows. Window 1 is between 7 and 9.5 microns, window 2 between 16 and 22 microns, "both windows" considers these windows concatenated together and the full spectrum uses all available data. The x-axis shows the absolute offset between the true temperature and predicted temperature, the y-axis shows the offset between the true and predicted column densities. The uncertainties in these values are not shown in the figure.

3.4.2 Subtracting known species

In this subsection, we aim to improve the estimates by removing known molecular emission of a spectrum to enhance the SO_2 emission and be able to search in the residual spectrum. As previously discussed, [16] reported column densities, temperatures, and emitting areas for a range of molecules in the GWLup disk. We generated the corresponding slab models for each of these species, except $^{13}CO_2$, and compared the resulting spectra to the GWLup spectrum. This comparison revealed a discrepancy between the two spectra. To address this, we applied a scaling factor to each species, adjusting it to best fit the data. This adjustment was achieved through a χ^2-fit using a model of the form $f(x) = \alpha x$, where x represents the intensity at a given point of the mock spectrum and $f(x)$ corresponds to the intensity of the target spectrum. The optimal value of the scalar factor, α, was determined through this fitting process. The values of these scaling factors are shown in Figure 17.
This discrepancy has been observed previously, and it is important to note that a single scaling factor does not result in a perfect match for each individual line in the mock spectrum of a single molecule. The differences likely arise from the method used to generate LTE slab models, with the most probable source of the discrepancy being the optical depth calculations, as discussed in [25].

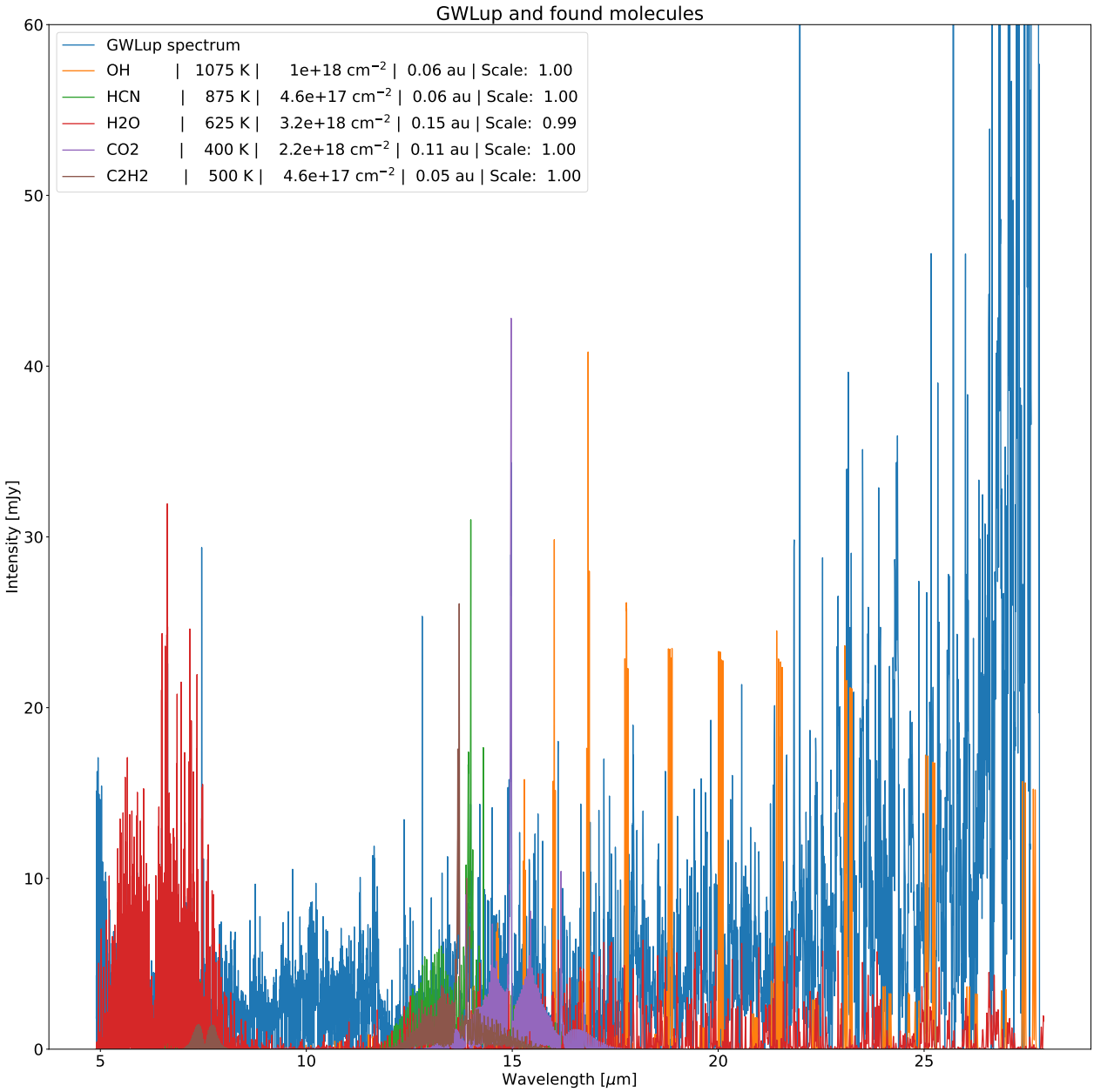

Figure 17: GWLup spectrum with scaled known species from [16]. Each scalar factor is found using a χ^2-fit to have the species-specific spectra match the observation. The spectrum is cut off below 0 and above 60 mJy to focus on the low-emission areas.

3.5 Identifying spectral windows based on dominant SO_2 emission

We also investigate which wavelength ranges might be optimal for observing a particular molecule, recognizing that this may vary with temperature. As an example, we consider a mock spectrum at 1600 K, with the following column densities, expressed in $\log_{10}$ base: CO: 20.0, CO_2: 14.0, H_2O: 18.0, NH_3: 17.0, OH: 15.0, and SO_2: 15.0. These values are typical based on the ranges reported in the literature.

We then examine all contiguous stretches of at least five data points where SO_2 has the highest intensity among the molecules. The threshold of five points is applied to exclude very short, anomalous

features in the wavelength ranges. This is less than the expected line width in a spectrum. Although the choice of this threshold is arbitrary, changing this value does not significantly affect the final spectral windows, as the windows are subsequently concatenated anyway.
This procedure yields a set of wavelength windows, at a given temperature, that are most suitable for detecting SO_2. The results for this specific example are presented in Figure 18.

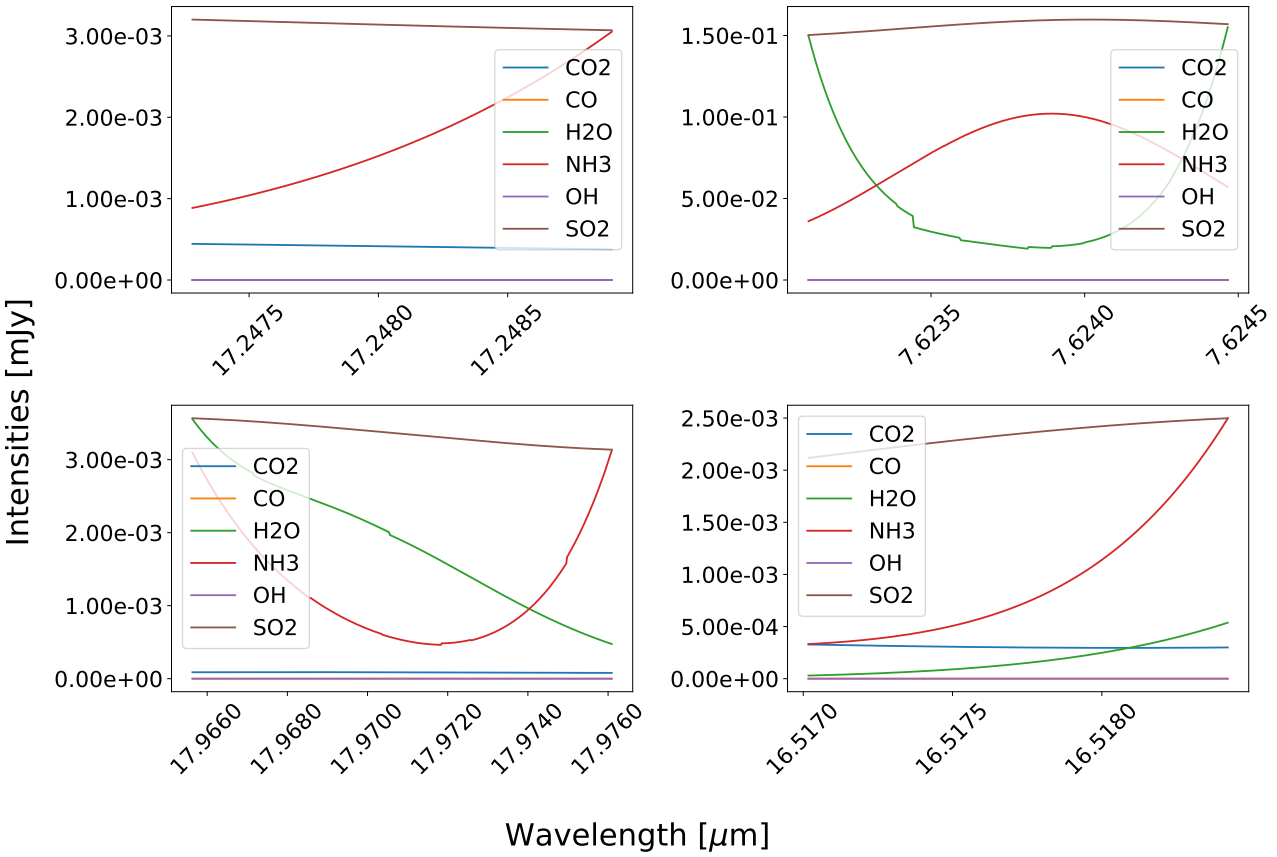

Figure 18: Wavelength windows suitable for detecting SO_2 at 1600K at reasonable wavelength values for each molecule involved. This figure only shows a subset of 4 windows, for illustrative purpose

We repeat this analysis for a range of reasonable column densities across temperatures between 100 K and 1200 K, in steps of 100 K. For each temperature, we identify the wavelength windows where SO_2 dominates the total intensity. We will then assess where these dominant ranges span approximately the same wavelength ranges across the different temperature models.
We filter out all windows where fewer than four model spectra at different temperatures exhibit SO_2 dominance, as such windows are deemed unreliable for detecting SO_2. The final spectral windows are presented in Figure 19.

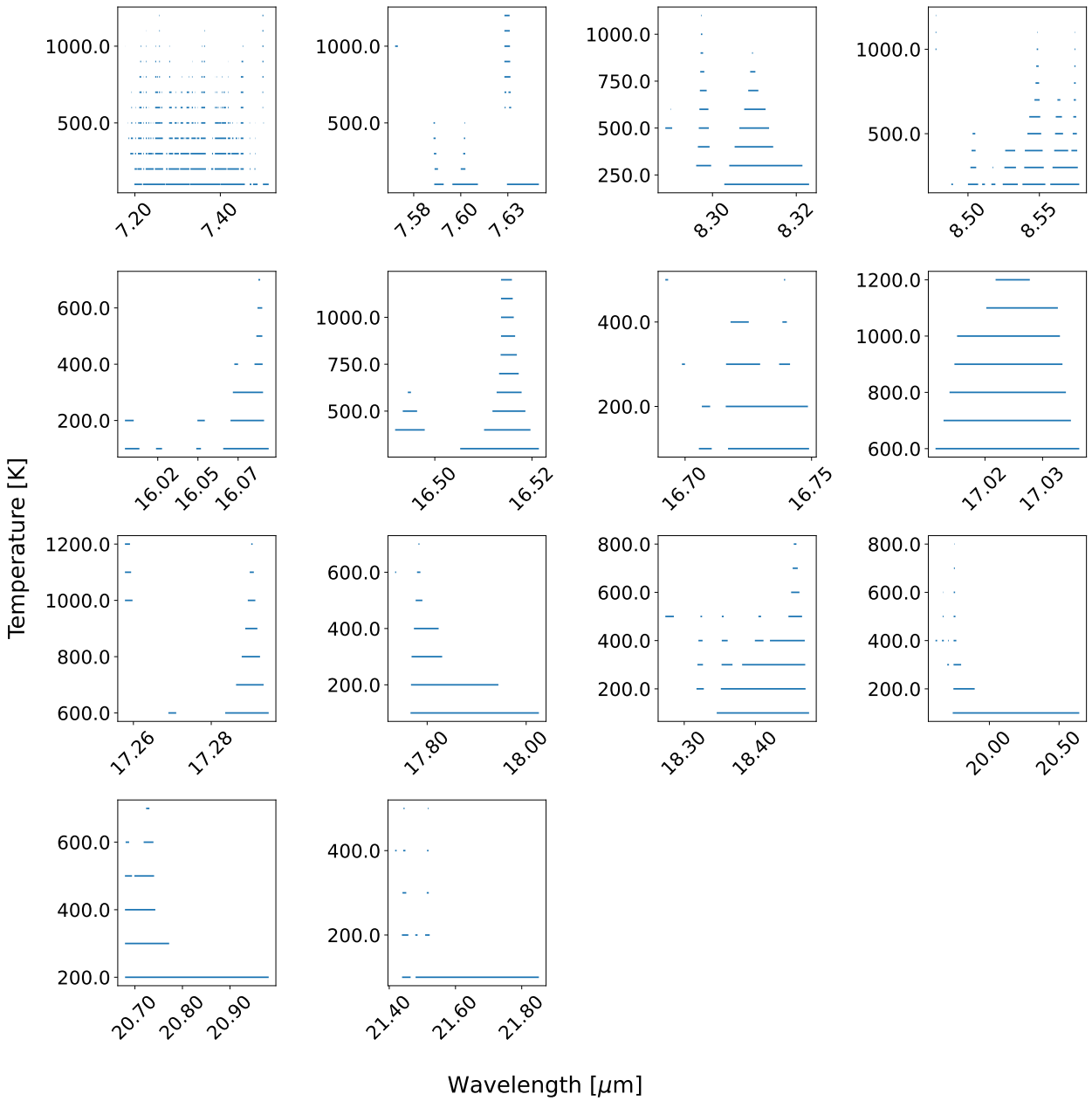

Figure 19: Wavelength windows where SO_2 dominates the intensity. For each temperature, the same column densities are taken. The x-axis shows the wavelength range of each window in microns and the y-axis the temperatures in Kelvin.

4 Results

To achieve the final results, a series of analyses were conducted, starting with testing the retrieval of SO_2 spectra from simulated debris disk observations by adding known spectra to a noise profile. The cross-correlation technique was used to match and evaluate the detectability of SO_2, considering both visual and algorithmic approaches. Next, the method was applied to spectra containing multiple species, scaled to match the GW Lup protoplanetary disk, with SO_2 added at varying signal-to-noise ratios to assess the reliability of temperature and column density predictions. Anomalies in predictions were investigated by isolating the effects of temperature and column density on SO_2 signals. Finally, the method was applied to the GW Lup spectrum itself, testing the detectability of SO_2 under realistic conditions, while also analyzing the thresholds needed for confident detection. These steps provided a comprehensive understanding of the limitations and potential of the approach.

4.1 Cross correlation performance and confirmation

4.1.1 Retrieving SO_2 from mock spectra

We first aim to evaluate whether known SO_2 spectra can be retrieved in the presence of a realistic noise profile. An example of such a spectrum is shown in Figure 10, which shows SO_2 added to a debris disk at a signal-to-noise ratio of 3, with the corresponding correlation matrix presented in Figure 11. To confirm the validity of an estimation, the mock spectrum based on the best estimate for our parameters is visually compared with the actual spectrum the estimate is for. The results for this example from Figure 10 are shown in Figures 20 and 21. In Figure 20, no peaks are observed to align with the expected positions, and this pattern persists when zooming in on the regions where SO_2 is expected to dominate. This indicates that, although the cross-correlation technique provides an accurate prediction, the presence of SO_2 is not visually discernible in the spectrum.

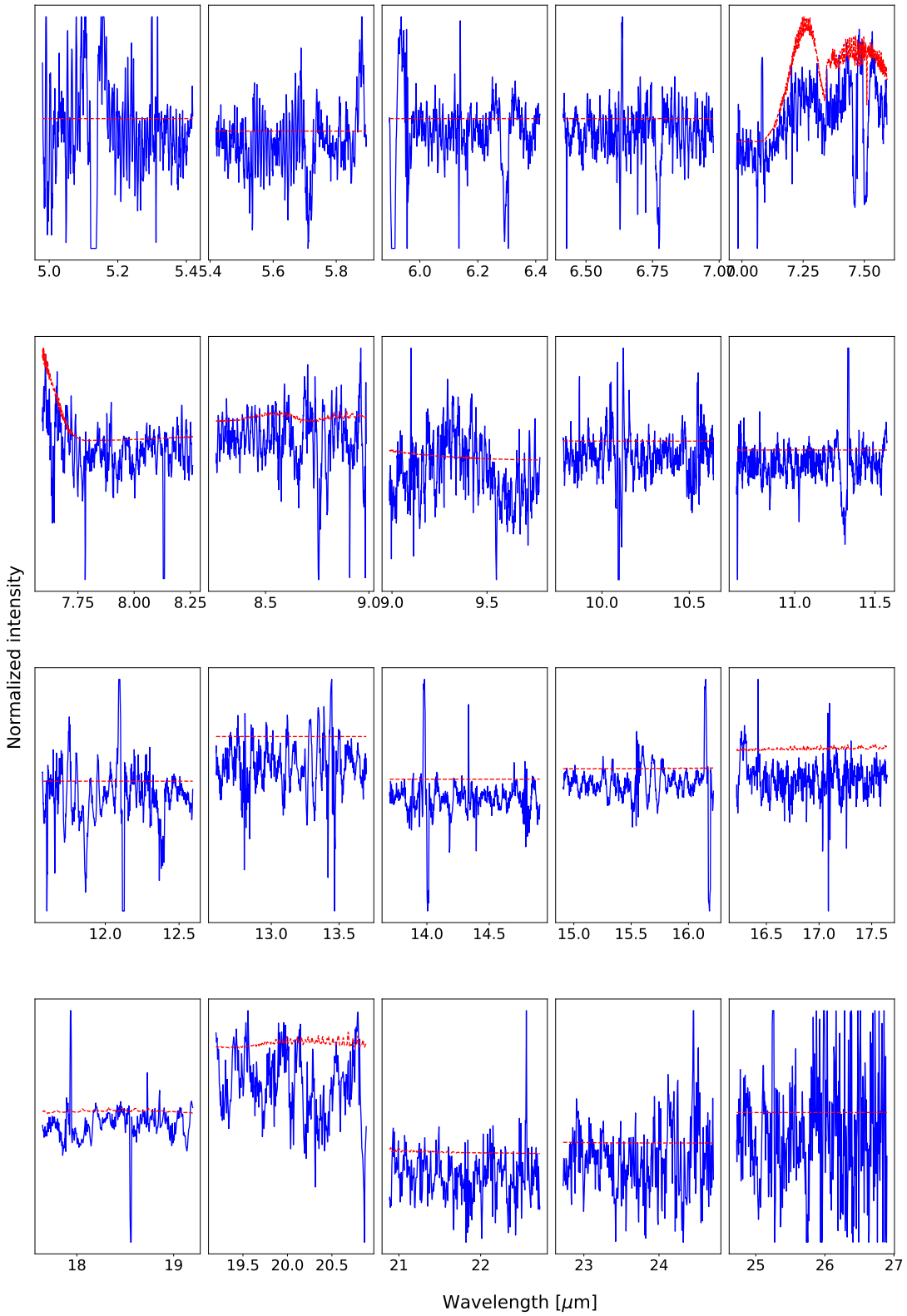

Figure 20: Mock SO_2 spectrum compared with the best matching SO_2 prediction, spliced in equally sized wavelength ranges. The scatters represent an algorithmic attempt at finding the peaks of the spectrum. The blue line shows a mock spectrum with SO_2 at 900 K with a column density of 10^{14}, the red shows the predicted SO_2 emission of 900 K and $10^{16.5}$ cm^{-2}.

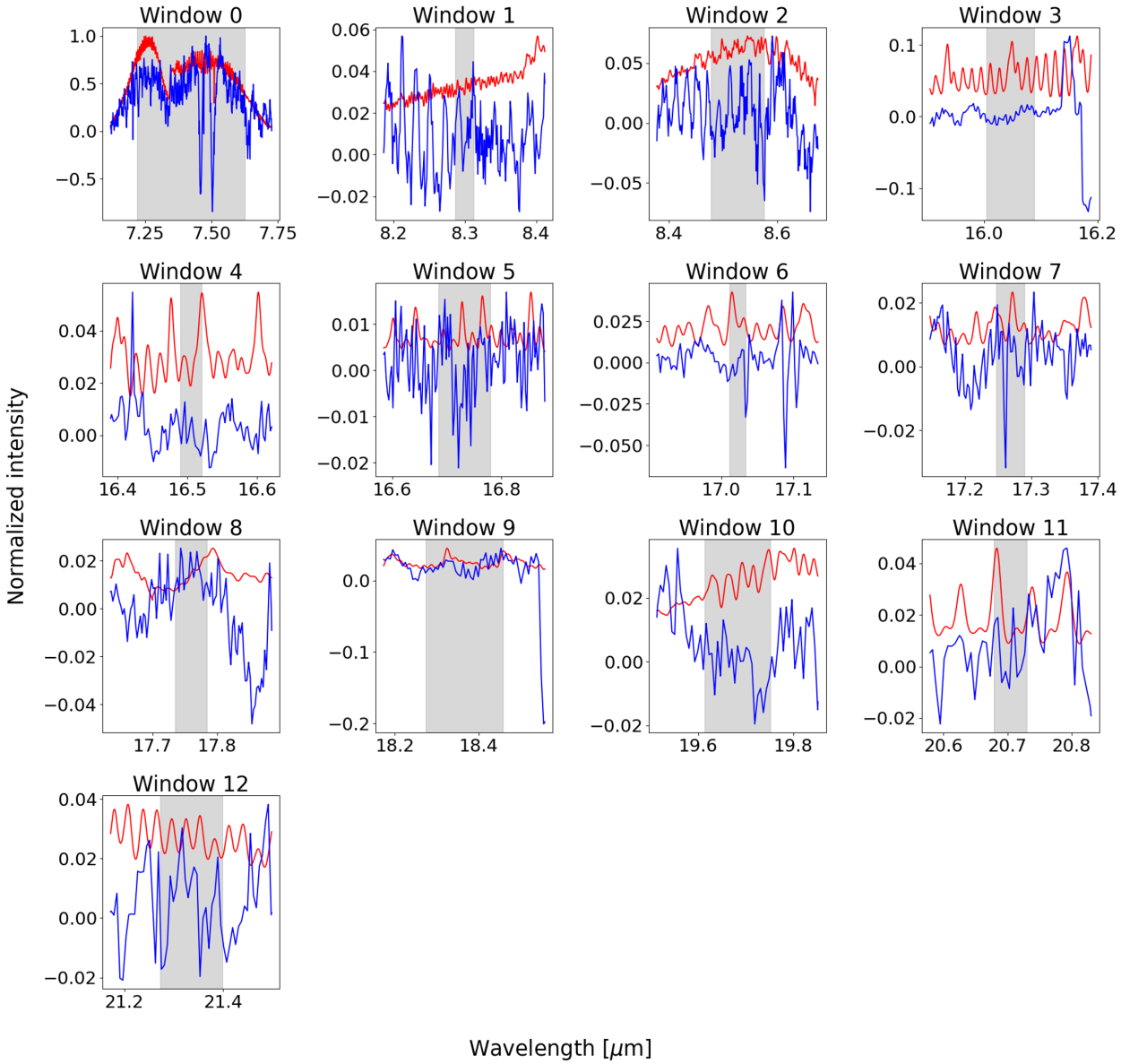

Figure 21: Mock SO_2 spectrum with SO_2 at 900 K with a column density of $10^{16.5}$ cm^{-2} compared with the best matching SO_2 prediction, shown around windows where SO_2 dominates the emission. The gray shaded area marks the wavelength range where the SO_2 intensity is expected to be higher than that of other species.

4.1.2 Cross correlation with mock spectra of multiple species

We took the obtained temperature, column density and emitting area estimates from [16], scaled to the GW Lup spectrum, and added SO_2 slab emission spectra at various temperatures and column densities. These spectra are not added based on signal-to-noise ratios, but rather on the fluxes obtained from prodimopy directly. One example of such a spectrum is shown in figure 22. This spectrum contains the species denoted in the legend, without a typical noise profile. When applying the cross-correlation method to obtain SO_2 temperature and column densities to the set of mock spectra, we observe the same estimates and thus the same predictions regardless of the input. We also see a correlation coefficient that is relatively high, which would mean a confident measurement. From this,

we can conclude that the method does not reliably work in every situation for finding SO_2. If the emitting area would increase or SO_2 would be scaled up higher, this could give better results from the method. This result likely differs a lot with the SO_2-only retrieval in the debris disk, as the ratio between the total spectrum flux and SO_2 emission spectrum flux here is much lower than the signal-to-noise ratios used with the debris disk, as the SO_2-spectrum is not scaled to a desired signall-to-noise value. To verify this, we will use the same method we did with creating mock spectra from the debris disk, but treat the debris disk with the known species corresponding to GWLup as the noise profile. We then add SO_2 at different signal-to-noise levels and determine for which SNR accurate predictions can be made. The results of this analysis are shown in table 3 and visualized in figures 23, 24 and 25. The threshold for the correlation coefficient to indicate a confident estimate is determined to be 0.19, which threshold is based on the calibration and can thus be used for any future measurements with this specific calibration input.

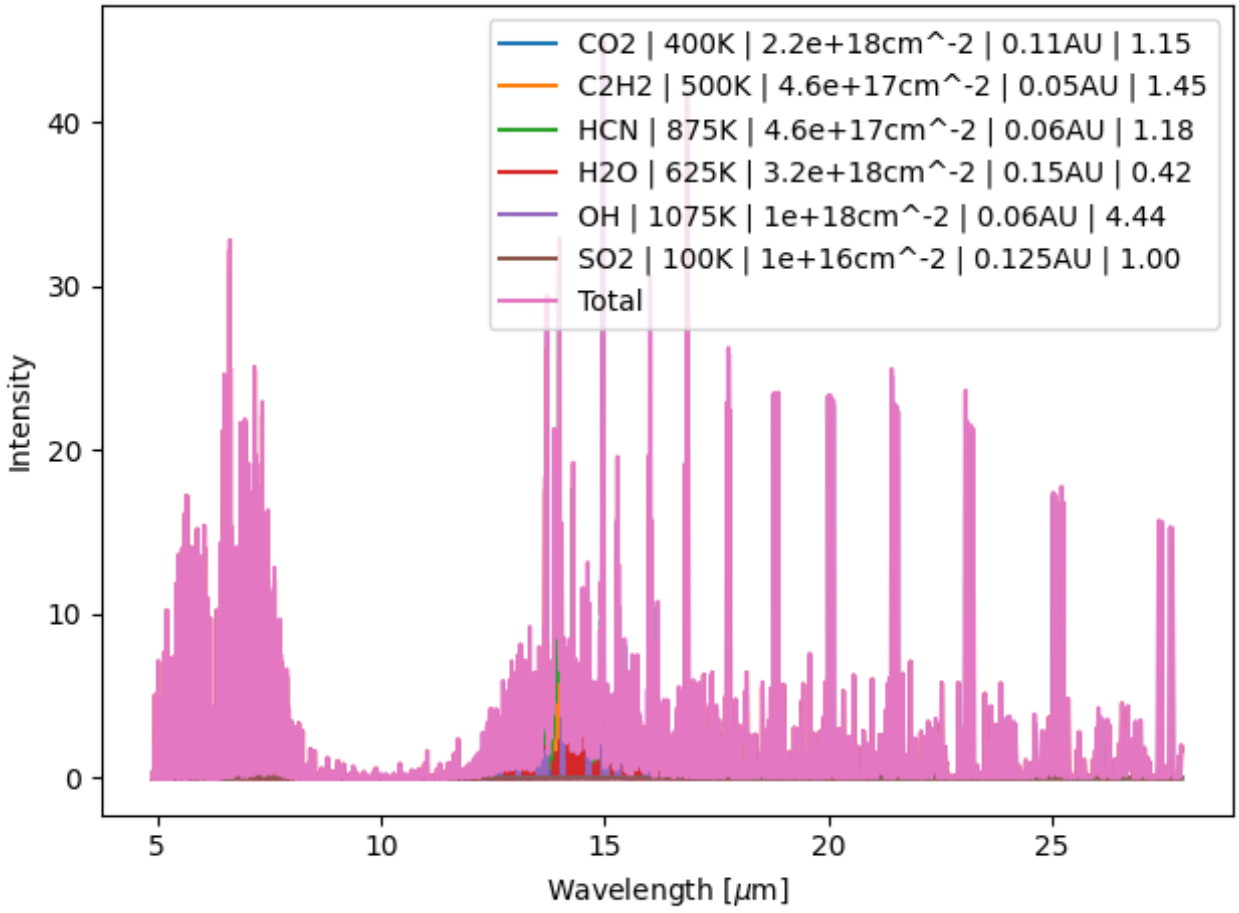

Figure 22: Model spectrum of GWLup species with SO_2 included. The legend denotes the species, temperature, column density, emitting radius, and scale factor respectively. The spectra are scaled such that the ProDiMo slab models match the GWLup spectrum with the temperatures, column densities and emitting areas found by [16]

SNR	temp_error_pred	temp_error_cal	dens_error_pred	dens_error_cal	obtained_corr
0.1	400.00	280.33	2.75	2.92	0.02
0.5	200.00	359.67	3.47	2.60	0.06
1.0	100.00	359.67	3.64	2.60	0.10
2.0	66.67	359.67	3.64	2.60	0.19
3.0	33.33	359.67	3.47	2.60	0.27
4.0	33.33	359.67	3.47	2.60	0.35
5.0	33.33	359.67	3.47	2.60	0.43
6.0	33.33	359.67	3.47	2.60	0.49

Table 3: Results of the SNR analysis, where the snr column denotes the signal-to-noise ratio at which the SO_2 spectrum is added to the noise profile consisting of the debris disk and model emission spectra of various species based on GW Lup. temp_error_pred is the mean offset between the predicted temperature and true temperature of all slabs considered at that SNR. temp_error_cal is the offset between calibrated temperature and true temperature. The dens columns are the same offsets for the column densities. The obtained_corr denotes the mean obtained correlation coefficient.

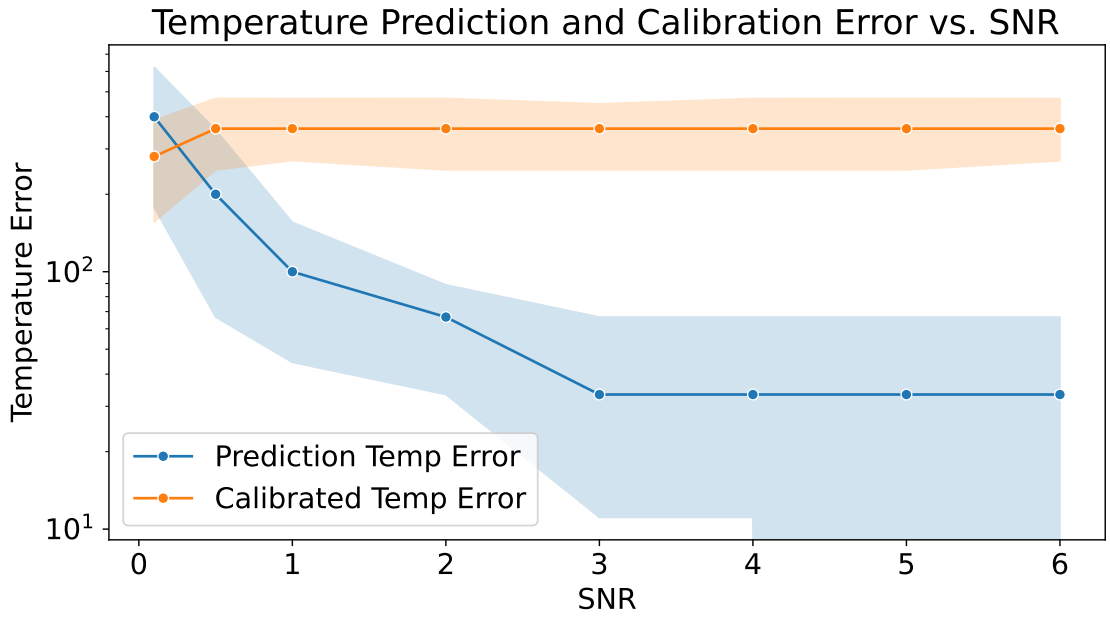

Figure 23: Calibration and prediction temperature versus the signal-to-noise ratio. The y-axis shows the mean offset between the true temperatures and the estimated temperatures of our sample spectra. The shaded region denotes the standard deviation of our 9 samples of mock spectra evenly distributed to cover the entire parameter space.

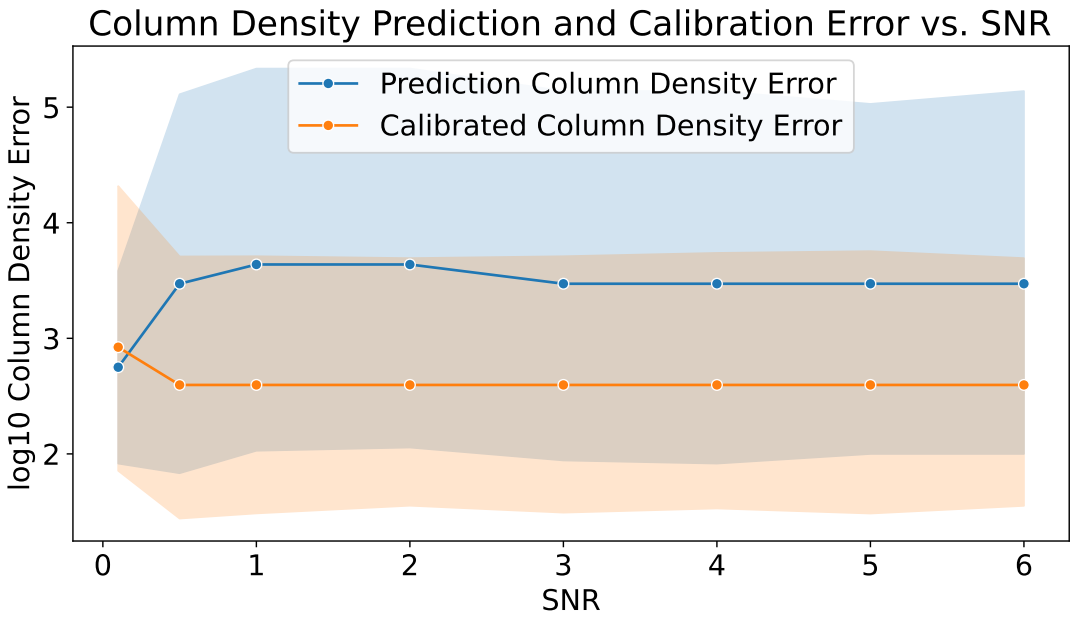

Figure 24: Calibration and prediction column densities versus the signal-to-noise ratio. The y-axis shows the mean offset between the true column densities and the estimated column densities of our sample spectra. The shaded region denotes the standard deviation of our 9 samples of mock spectra evenly distributed to cover the entire parameter space.

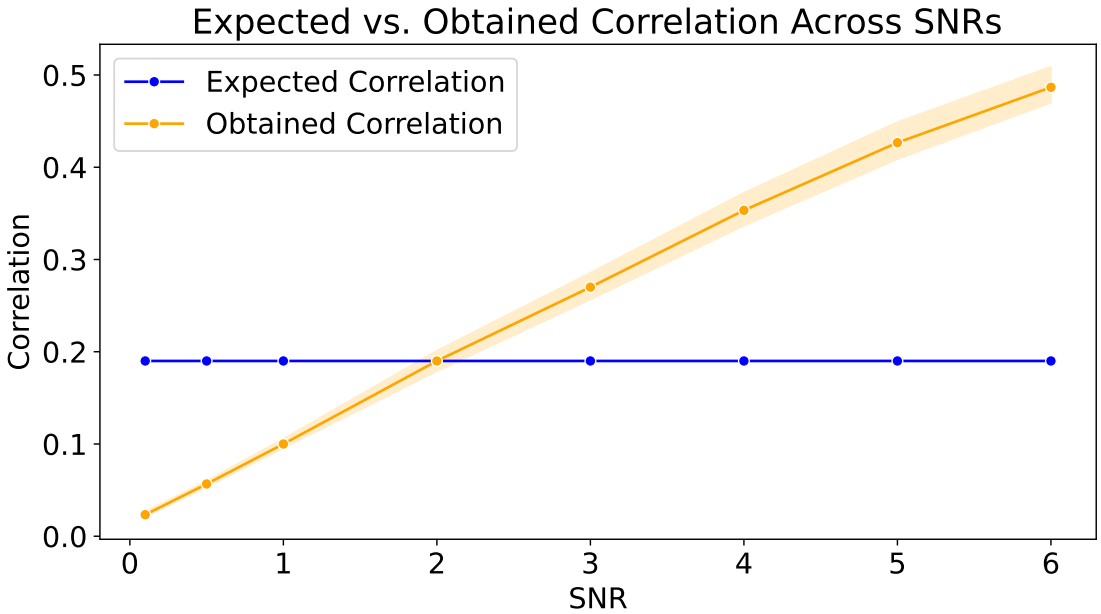

Figure 25: Expected and obtained correlation coefficients as a function of the signal-to-noise ratio. The expected correlation coefficient (blue) is the threshold above which we expect a valid measurement. The obtained correlation coefficient (orange) shows the mean correlation coefficient of our 9 sample spectra of mock spectra evenly distributed to cover the entire parameter space, with the shaded region denoting the standard deviation.

Figures 23, 24 and 25 show that we require a signal-to-noise ratio of at least 2 to make a confident

prediction of SO_2. Temperature predictions are reasonably accurate at a signal-to-noise ratio of 1 but become unreliable at 0.5, making an SNR threshold of 2 a justified and reliable benchmark for SO_2 detection. We also see that the temperature is better estimated from the prediction rather than the calibration, contrary to the results we observed from SO_2-only simulations, while the column density predictions are still better from calibration measurements. This likely means the SO_2-only calibration cannot be generalized that well. The expected correlation coefficient above which we expect a confident measurement is constant, as we use the same calibration file for all measurements as described previously.

4.2 Cross correlation limitations

4.2.1 Explaining prediction anomalies

When analyzing the results of various observations, we notice some strange phenomena that although we can process them, we would like to understand why they occur. For example, a temperature of 100 K with a column density of $10^{4.5}$ cm^{-2} gives a consistently high correlation coefficient. We also observed an increase in offsets toward the lower bound of the parameter space, but not at the other bounds. To explain this, we need to understand the effects of changing temperature and column density separately, as visualized in Figures 27 and 26. In these figures, we see that at a temperature of 100 K, we see no signal at all in the first band, between 7 and 9.8 microns, and only in the second (15-22.5 μm) do we observe very small, but almost no fluctuations in the SO_2 emission flux. At 200 K, we already do see signals in both these wavelength ranges, although weakly. With constant temperature, we see that at a column density of 10^5 cm^{-2} we see no signal at all. In real observations, we can expect column densities below around 10^{10} to be indistinguishable from noise, as the ratio to other species becomes too large. To get an observable signal, we would have to scale up the emitting area to several astronomical units, which is unrealistic for a typical protoplanetary disk [25]. Because of this, it could be considered to remove all column densities below a certain threshold from the evaluation, as to avoid skewing other results. Since we see no emission from column densities below 10^7, these parts of earlier grids should be ignored.

We also observe that changing the column density seemingly scales the relative heights of the peaks in the emission spectra, without introducing other differences between the cases. For temperatures we do see differences, which can for example be seen around 7.6 microns. Because mock spectra are normalized, the relative peak height variations induced by temperatures are preserved, but the scaling due to column density is lost, which is most likely why temperature estimations are far more accurate than column density predictions.

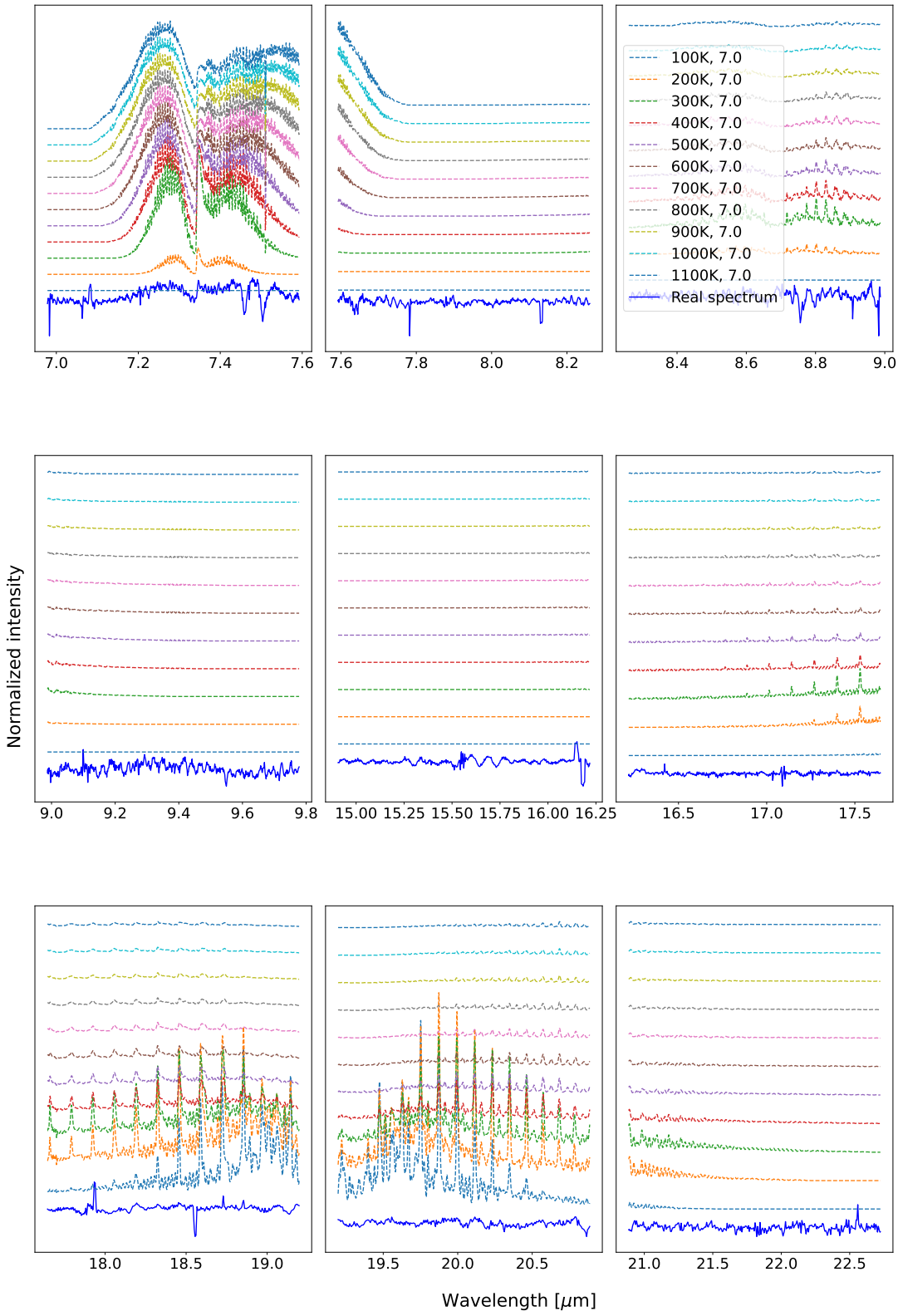

Figure 26: SO_2 spectrum with overplots of various slab models with the same temperature and varying column densities. The blue line shows a mock spectrum simulating a real observation at a temperature of 500 K and a column density of 10^7 cm^{-2}.

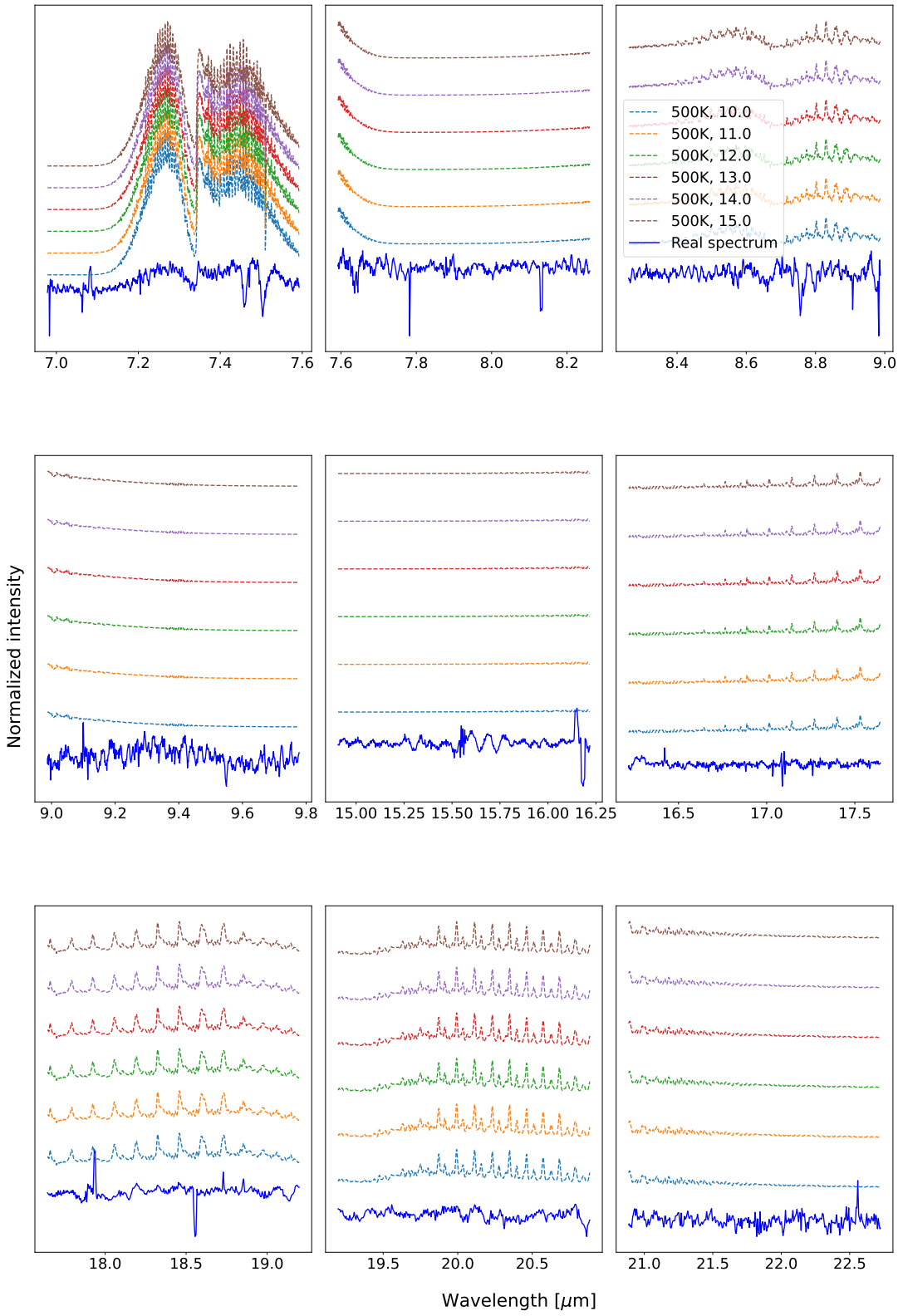

Figure 27: SO_2 spectrum with overplots of various slab models with the same column density and varying temperatures. The blue line shows a mock spectrum simulating a real observation at a temperature of 500 K and a column density of 10^7 cm^{-2}.

4.3 SO_2 in GWLup

We applied the method to the full GWLup spectrum to see whether we could find traces of SO_2 in this protoplanetary disk. However, we got no matches with a cross-correlation coefficient above 0, thus no valid measurement of SO_2.
We then produced a residual spectrum by subtracting the emission from known species from the total spectrum as shown in figure 17, which could make it easier to search for SO_2. Again, we got no measurements with a positive correlation coefficient, meaning if there is SO_2 in the spectrum, its signal is not strong enough for us to detect using this method.
From the results in Section 4.1.2, we know we can expect to see SO_2 if its spectrum achieves a higher signal-to-noise ratio than 2. So we can compute what column densities and temperatures this would require at different emitting areas. The results of this are shown in figures 28, 29, 30, and 31. We see that given a column density and temperature, a larger emitting area results in a higher SNR of SO_2. Increasing the temperature and column density also increases the obtained SNR.

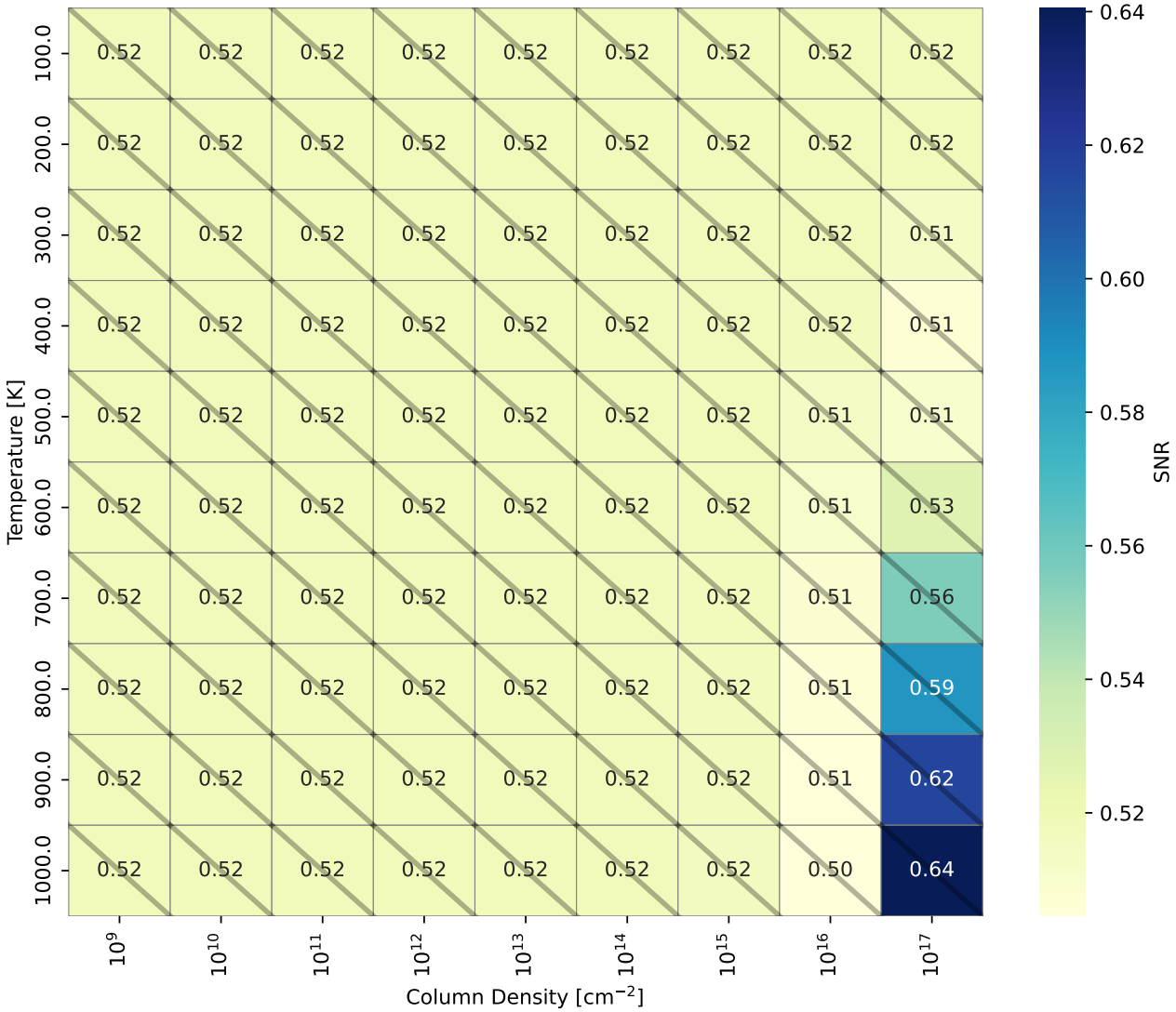

Figure 28: Signal-to-noise ratios obtained for different combinations of column density and temperature with an emitting radius of 0.1 AU. The diagonal stripes mark the models obtaining an SNR below the established threshold of 2.

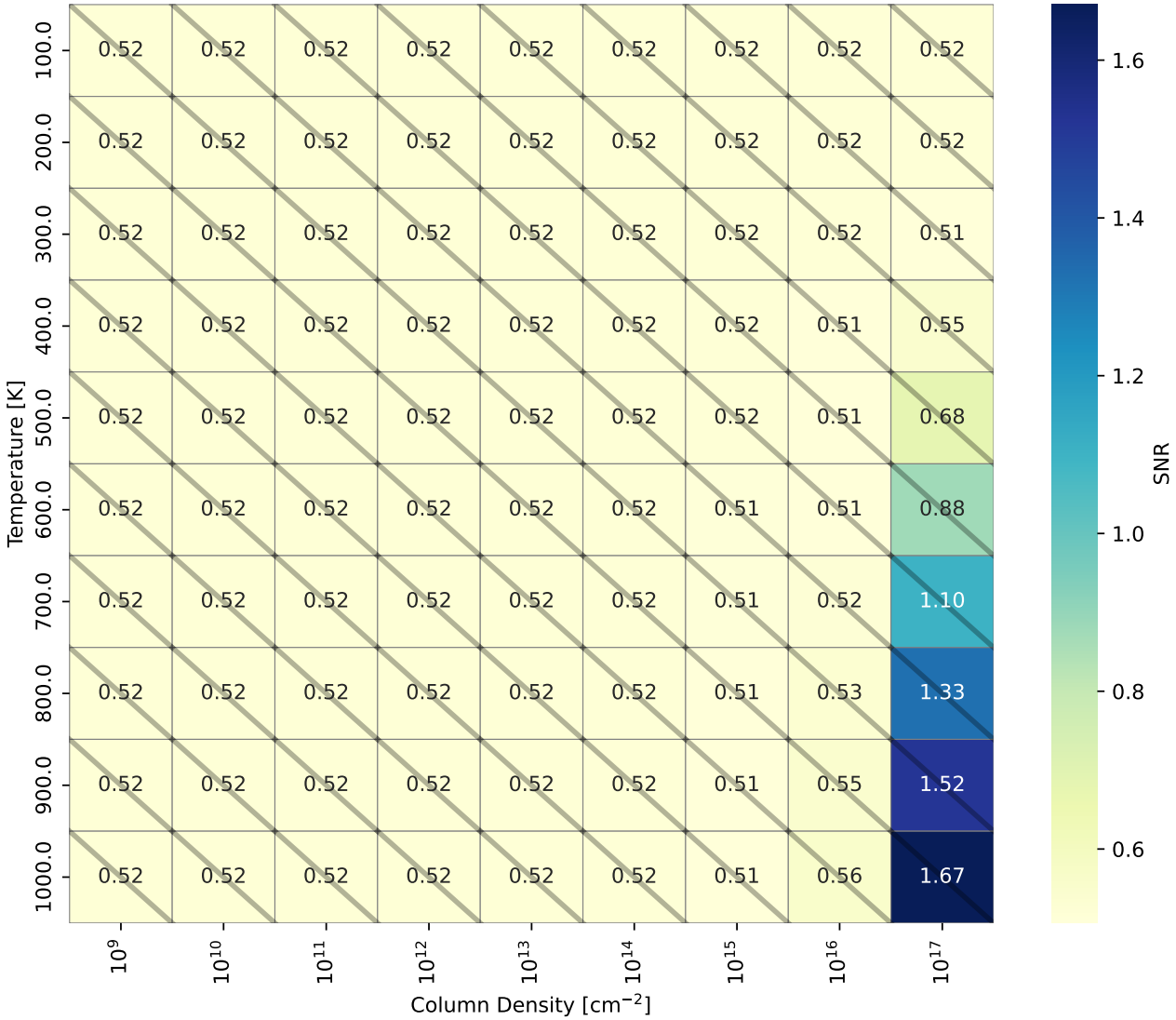

Figure 29: Signal-to-noise ratios obtained for different combinations of column density and temperature with an emitting radius of 0.3 AU. The diagonal stripes mark the models obtaining an SNR below the established threshold of 2.

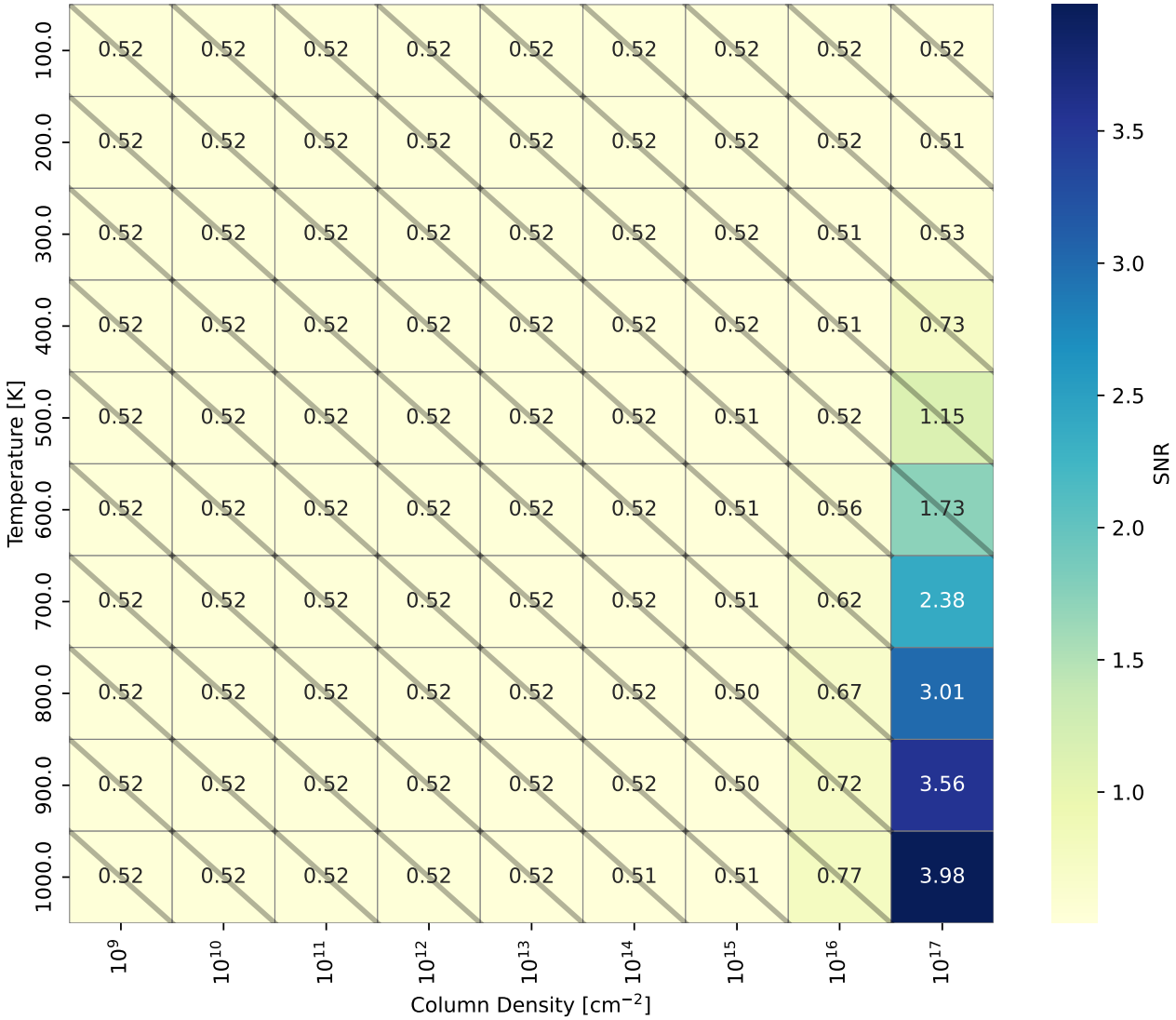

Figure 30: Signal-to-noise ratios obtained for different combinations of column density and temperature with an emitting radius of 0.5 AU. The diagonal stripes mark the models obtaining an SNR below the established threshold of 2..

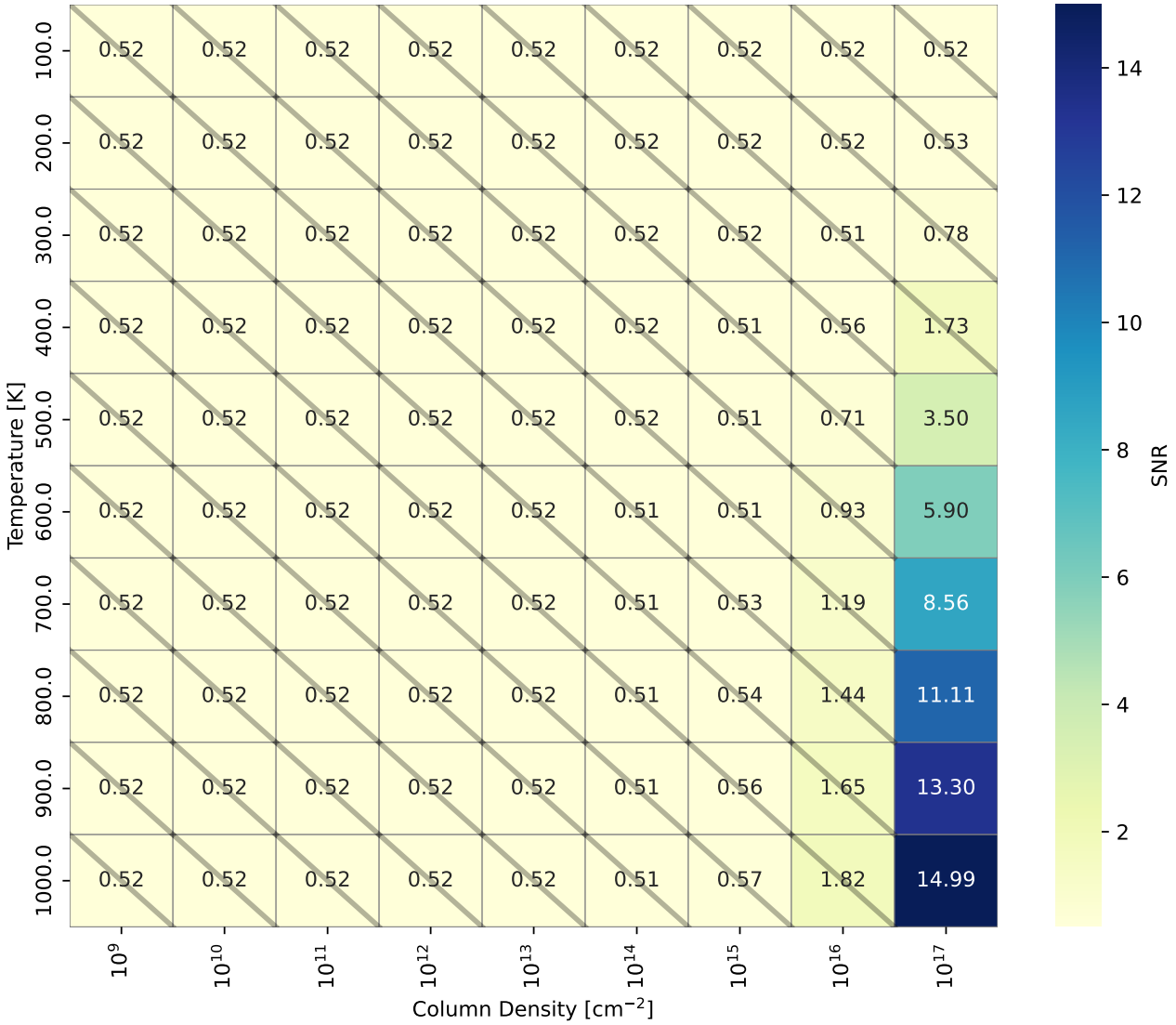

Figure 31: Signal-to-noise ratios obtained for different combinations of column density and temperature with an emitting radius of 1 AU. The diagonal stripes mark the models obtaining an SNR below the established threshold of 2.

We want to compare these results to those obtained by the same analysis, except only using the mock spectra consisting of the typical noise spectrum and the SO_2 emission spectrum. This way, more insight into the origin of this high threshold can be obtained. The results of this analysis can be found in appendix B. We observe minimal differences in the comparison between the predicted and calibrated estimates of the temperature and column density. The expected and obtained correlations between signal-to-noise ratios looks almost identical, resulting in the same threshold value of 2 for this type of mock spectrum. Analyzing the combinations of column density and temperature for which we predict SO_2 to be observable, we see that the signal-to-noise ratio increases faster for the mock spectra with only SO_2, but how this value increases seems similar. Thus we can conclude that the other species make the SO_2 signal harder to observe, but the signal will not be lost by other species.

5 Discussion and Conclusion

5.1 Summary of the cross-correlation method to search for new molecules

In this thesis, we developed a method for detecting new molecules in a JWST MIRI MRS spectrum. We focussed on SO_2 detection in protoplanetary disks, as this could give more insight into the origin of the so-called sulfur depletion problem. The method generates a cross-correlation matrix using a grid of SO_2-only spectra with varying combinations of column density and temperature, and correlating this with the target spectrum. From this, the best matches are obtained and possible outliers are processed, after which the most likely true estimate for the temperature and column density of the species is estimated using a weighted average of the k nearest neighbors in a precomputed calibration grid. This also yields a measurement of uncertainty in our estimation. The estimation can be verified by visually comparing the best-matching SO_2-only spectrum with the target spectrum and determining whether the SO_2 peaks are present in the target. This visual confirmation can be performed both in the windows where SO_2 is shown to dominate the intensity in ProDiMoPy simulations of 0D slab models, or across the entire wavelength range. We have applied the method on GWLup and established a threshold of temperature and column density combinations at various SO_2 emitting areas, but were unable to observe SO_2 in GWLup. We were able to conclude that the impact of other species in the case of GWLup does not completely prevent us from detecting the SO_2 signal, but the signal-to-noise ratio required is higher.

5.2 Limitations of the method

The method we developed shows varying behavior for different cases, where we considered mock spectra with only SO_2 and with SO_2 and other species. For retrieving SO_2 back from a debris disk at different signal-to-noise levels, we observed the calibration to result in the best measurement. However, for the same method applied to a debris disk with species corresponding to GWLup added in, we saw temperature estimations to be better based on the prediction rather than the calibrated values, while column density estimations are still better using the calibration method. Overall, we noticed we can make fairly accurate temperature predictions, but the uncertainty in column density estimations remains too large to be meaningful. When applying the method on GWLup, an actual spectrum of a protoplanetary disk, we are unable to detect SO_2, meaning the signal of SO_2 compared to the rest of the spectrum is too low. We have established rough thresholds above which we would expect a detection for column density and temperature combinations at various emitting areas for GWLup, which show that SO_2 is most likely only observable at very high temperatures (700+ K) and column densities (10^{17} cm^{-2}) for this specific example, which is an unlikely scenario. For the mock spectra containing no other species besides SO_2, we observe a higher signal-to-noise under the same conditions compared to the mock spectra with other species included at high temperature and column density. At the low end of the spectrum we see a lower signal-to-noise, indicating that part of the emission spectrum of other species returns false positives for SO_2 emission, but not enough for the cross-correlation method to detect this false positive as the presence of SO_2 emission.

5.3 Future Work

5.3.1 Obtaining more accurate estimates

Several improvements could be made to our method for obtaining the SO_2 temperature and column density, which are used to visually determine the presence of SO_2 in a spectrum by generating a model

spectrum with these parameters and comparing the emission peaks with the observed data.
The dataset of SO_2-only spectra only takes a discrete set of combinations of these parameters. This combination is also used for the calibration and cross-correlation and thus strongly impacts the final estimate. A more dense dataset could be used to get a finer measurement, which could further solidify or enhance the values of various thresholds used throughout the method. The quality of the dataset could also be improved to better resemble JWST spectra. For example, the method currently handles the resolving power in chunks representing the different channels of the instrument, but the literature shows that this method is not perfectly accurate. If the spectral resolution could be handled using a smooth function of wavelength, or in smaller chunks, the method could obtain better predictions. Lastly, the generated slab models could be replaced by more accurate models, such as those that include radial temperature and column density changes. This would require more computing power but also could give a higher accuracy for our results.
In attempting to retrieve SO_2 from sample spectra with other species added in, we use a selected set of species from which we attempt to retrieve the SO_2. This set does not include all species that can affect the final estimate from our method. Further analysis could be done to determine which species most affect our ability to retrieve SO_2. When trying to find SO_2 in the GWLup spectrum, we attempt to remove some species, but other molecules are not taken into account and might still affect the performance of our method. The method of removing species can also affect the SO_2 signal, so a better method of removing the data should be developed that perhaps adjusts the signal on a line-by-line basis.
Another point that could be worth investigating is whether calibration including known species would work better for observations where composition data is known. We have seen SO_2-only calibrations do not generalize well for temperature estimations, so perhaps this estimate can be improved by making more tailored calibrations.

5.3.2 Applicability to other species

The entire method is made such that it is as flexible as possible. As long as sufficient spectral data is available, the method should apply to any species. This would require new calibrations and new refinement of certain thresholds. It could also be applied to the species that strongly blend SO_2, such as H_2O or CO_2, to find a good estimate and remove these molecules before determining SO_2. However, this does mean we would need accurate predictions of the column density and emitting area, so this possibility needs to be investigated further. Another thing to consider is the required signal-to-noise ratio for observability, and whether we can expect observations with reasonable values for a given species.

5.3.3 Other considerations

We first estimated the viability of the model by retrieving SO_2 from the debris disk at various signal-to-noise ratios, where the debris disk resembles a typical noise profile of a JWST observation. However, this noise profile is not a constant that can easily be removed from an observation. It could be worth investigating how this noise profile changes over time and whether it is always viable to retrieve SO_2-only spectra from a noise profile.
It would be reasonable to assume the observability of SO_2 to decrease with column density after a certain point, due to changes in the optical depth. This could also explain the differences between the obtained LTE slab models between ProDiMoPy and [16]. This behavior is also seen in how the required signal-to-noise ratio evolves with emitting area and thus could be worth examining further.

References

[1] R. Martín-Doménech et al. *The sulfur depletion problem: Upper limits on the H2S2, HS·2, and S2 gas-phase abundances toward the low-mass warm core IRAS 16293-2422*. Jan. 2016. URL: https://www.aanda.org/articles/aa/full_html/2016/01/aa26271-15/aa26271-15.html.

[2] Jelke Betlehem. June 2022. URL: https://fse.studenttheses.ub.rug.nl/27788/1/Master_Thesis_Astronomy_Jelke_Bethlehem.pdf.

[3] A. Jiménez-Escobar and G. M. Muñoz Caro. *Sulfur depletion in dense clouds and circumstellar regions - i. h2s ice abundance and UV-photochemical reactions in the H2O-matrix*. Dec. 2011. URL: https://www.aanda.org/articles/aa/full_html/2011/12/aa14821-10/aa14821-10.html.

[4] A.C.A. Boogert et al. Mar. 1996. URL: https://articles.adsabs.harvard.edu/cgi-bin/nph-iarticle_query?db_key=AST&bibcode=1997A%26A...317..929B&letter=0&classic=YES&defaultprint=YES&whole_paper=YES&page=929&epage=929&send=Send+PDF&filetype=.pdf.

[5] D. Semenov et al. *Chemistry in disks - XI. sulfur-bearing species as tracers of protoplanetary disk physics and chemistry: The DM tau case*. Sept. 2018. URL: https://www.aanda.org/articles/aa/full_html/2018/09/aa32980-18/aa32980-18.html.

[6] STSci. *JWST User Documentation*. Aug. 2024. URL: https://jwst-docs.stsci.edu/jwst-mid-infrared-instrument#gsc.tab=0.

[7] STSci. *JWST User Documentation*. July 2024. URL: https://jwst-docs.stsci.edu/jwst-mid-infrared-instrument/miri-observing-modes/miri-medium-resolution-spectroscopy#gsc.tab=0.

[8] Karin I. Öberg, Stefano Facchini, and Dana E. Anderson. *Protoplanetary Disk Chemistry*. Sept. 2023. URL: https://arxiv.org/abs/2309.05685.

[9] Sean M. Andrews. *The structures of protoplanetary disks*. Aug. 2021. URL: https://pubs.aip.org/physicstoday/article/74/8/36/837483/The-structures-of-protoplanetary-disksAstronomical.

[10] P. Christian Schneider, H. Moritz Günther, and Kevin France. *The UV Perspective of Low-Mass Star Formation*. 2020. URL: https://dspace.mit.edu/bitstream/handle/1721.1/150608/galaxies-11-00061-v2.pdf?sequence=1&isAllowed=y.

[11] Danny Gasman et al. *Minds. abundant water and varying C/O across the disk of SZ 98 as seen by JWST/Miri*. Oct. 2023. URL: https://arxiv.org/abs/2307.09301.

[12] C. Salyk et al. *A Spitzer survey of mid-infrared molecular emission from Protoplanetary Disks II: Correlations and LTE models*. Apr. 2011. URL: https://arxiv.org/abs/1104.0948.

[13] I. Kamp et al. *Consistent dust and gas models for protoplanetary disks - II. Chemical Networks and rates*. Nov. 2017. URL: https://www.aanda.org/articles/aa/full_html/2017/11/aa30388-17/aa30388-17.html.

[14] Inga Kamp, Peter Woitke, and John D. Ilee. *Sumer School "Protoplanetary Disks: Theory and Modelling Meet Observations"*. EPJ web of conferences, 2014.

[15] Cornelis P Dullemond. 2013. URL: https://www.ita.uni-heidelberg.de/~dullemond/lectures/leshouches2013.pdf.

[16] Sierra L. Grant et al. *Minds. the detection of $^{13}CO_2$ with JWST-Miri indicates abundant CO_2 in a protoplanetary disk*. Apr. 2023. URL: https://arxiv.org/abs/2212.08047.

[17] Gabriela Diaz. *Wavelength to energy calculator*. Apr. 2024. URL: https://www.omnicalculator.com/physics/wavelength-to-energy.

[18] Libretexts. Feb. 2024. URL: https://chem.libretexts.org/Bookshelves/Physical_and_Theoretical_Chemistry_Textbook_Maps/Supplemental_Modules_%28Physical_and_Theoretical_Chemistry%29/Spectroscopy/Rotational_Spectroscopy/Rovibrational_Spectroscopy.

[19] Libretexts. *Anharmonic oscillator*. Jan. 2023. URL: https://chem.libretexts.org/Bookshelves/Physical_and_Theoretical_Chemistry_Textbook_Maps/Supplemental_Modules_(Physical_and_Theoretical_Chemistry)/Quantum_Mechanics/06._One_Dimensional_Harmonic_Oscillator/Anharmonic_Oscillator.

[20] Christian Hill. URL: https://hitran.org/.

[21] Aditya M. Arabhavi and Inga Kamp. *Adityamarabhavi/astrochemschool2024*. 2024. URL: https://github.com/adityamarabhavi/astrochemschool2024/tree/master.

[22] Christian Rab. *Prodimopy*. 2017. URL: https://prodimopy.readthedocs.io/en/stable/.

[23] STSci. *JWST User Documentation*. Aug. 2024. URL: https://jwst-docs.stsci.edu/methods-and-roadmaps/jwst-time-series-observations/jwst-time-series-observations-noise-sources#gsc.tab=0.

[24] STSci. *JWST User Documentation*. July 2024. URL: https://jwst-docs.stsci.edu/jwst-mid-infrared-instrument/miri-observing-modes/miri-medium-resolution-spectroscopy#MIRIMediumResolutionSpectroscopy-wavelengthMRSwavelengthcoverageandspe

[25] I. Kamp. *Private correspondence*. Sept. 2024.

[26] scipy. *Pearsonr*. 2024. URL: https://docs.scipy.org/doc/scipy/reference/generated/scipy.stats.pearsonr.html.

A Appendices

A.1 Protoplanetary disk model

In this section, two derivations for protoplanetary disk models are derived following [14, 15]. The first section shows only radial change, whereas the second model also takes into account vertical dependence.

A.1.1 Derivations for the radial variation

The structure of a disk can be described by general equations. We will first look at the steady-state disk structure, assuming radial and angular momentum conservation, and vertical hydrostatic equilibrium. We then consider a disk annulus at a distance r from the star with material flowing in and out of the annulus with velocity v_r in the radial direction. The radial momentum conservation can then be written as

$$v_r \frac{\partial v_r}{\partial r} - \frac{v_\phi^2}{r} + \frac{1}{\rho_{\text{gas}}} \frac{\partial P}{\partial r} + \frac{GM_*}{r^2} = 0, \tag{19}$$

with v_ϕ the circular velocity, P the gas pressure, ρ_{gas} the gas density and M_* the mass of the central star. The sound speed of the gas is defined as $c_s = \frac{\partial P}{\partial \rho_{\text{gas}}}$. Assuming an ideal gas, $c_s = \sqrt{\frac{kT_g}{\mu m_p}}$ with k the Boltzmann constant, T_g the gas temperature, μ the mean molecular weight and m_p the proton mass. Conservation of angular momentum follows from the assumption of a steady state and the definition of torque, resulting in

$$\frac{\partial}{\partial r}(r v_r \Sigma r^2 \Omega) = \frac{\partial}{\partial r}(\nu \Sigma r^3 \frac{d\Omega}{dr}), \tag{20}$$

where the l.h.s. shows the radial change in angular momentum and the r.h.s is a result of viscous torques. Σ is the surface density of the gas, $v_\phi = r\Omega$ with Ω the angular velocity, and ν the kinematic viscosity. The kinematic viscosity is a measure of a fluid's resistance to flow under gravitational forces and is often calculated as the ratio between the dynamic viscosity and volume density. Integrating this and assuming the disk extends to the star, we get

$$\Sigma(r) = \frac{\dot{M}}{3\pi\nu}(1 - \sqrt{\frac{R_*}{r}}), \tag{21}$$

which is valid for radii much larger than the stellar radius. Note that ν is not constant in the equation, but $\dot{M} = 2\pi r \Sigma(-v_r)$ is.
The vertical disk structure is found by solving the equation for hydrostatic equilibrium. Assuming an ideal gas, this results in the gas scale height given by

$$H_{\text{gas}} = \sqrt{\frac{kT_c r^3}{\mu m_p G M_*}}, \tag{22}$$

where T_c is the gas temperature at the midplane. This is a simplified result assuming T_g and μ are constant with the vertical height z, which in reality does not have to be the case.
If we parametrize the viscosity $\nu = \alpha c_s H_{\text{gas}}$ and assume $r >> R_*$, we find

$$\Sigma = \frac{\mu m_p \sqrt{GM_*}}{3\pi k} \frac{\dot{M}}{\alpha T_c r^{3/2}}. \tag{23}$$

Then assuming a simple power law for the midplane temperature, thus $T_c \propto r^{-q}$, we get a surface density $\Sigma \propto r^{q-3/2}$, thus also a simple power law.
By looking at the mass distribution in the solar system, the minimum amount of matter in the disk at formation can be inferred. This leads to the Minimum Mass Solar Nebula (MMSN) model. The results of this model are often structured in the following way:

$$\Sigma_{\text{gas}}^{\text{MMSN}}(r) = 1700(\frac{r}{1\text{AU}})^{-3/2}, \tag{24}$$

$$\Sigma_{\text{dust}}^{\text{MMSN}}(r) = 7(\frac{r}{1\text{AU}})^{-3/2}, \tag{25}$$

$$\Sigma_{\text{ice}}^{\text{MMSN}}(r) = 22(\frac{r}{1\text{AU}})^{-3/2}, \tag{26}$$

where Σ is the surface density in g cm^{-2}. Note for ice we assume it only to be present for $r > 2.7$ AU, which is the so-called snow-line [15].
We can then write the midplane density ρ_c as

$$\rho_c \approx \frac{\Sigma}{H_{\text{gas}}} = \rho_{\text{in}}(\frac{r}{r_{\text{in}}})^{\frac{3}{2}q-3}, \tag{27}$$

with ρ_{in} the density at the inner disk radius r_{in}. This is assuming the simple power law for the temperature profile. This can actually be verified by looking at the energy generation, which is predominantly due to viscous torques. Assuming the energy generated is not transported in the disk, but radiated away locally through its two surfaces, and assuming the disk has a Keplerian rotation profile, thus $\Omega = \sqrt{\frac{GM_*}{r^3}} = \Omega_K$, we get a temperature profile of

$$T_{\text{disk}} = (\frac{3}{8\pi\sigma}\dot{M}\Omega^2)^{1/4}, \tag{28}$$

where T_{disk} is the effective temperature of the disk, assuming the disk is predominantly heated by viscous dissipation and thus ignoring radiation effects, and σ the Stefan-Boltzmann constant. Note that this temperature profile does not depend on viscosity. The model based on these equations is visualized in figures 1 and 2, which are based on the same model and visualize the same PPD in different ways. For a disk in a viscous-heating-only model, $T_c \propto T_{\text{disk}}$.

A.1.2 Model with vertical dependence

Like with the radial structure, the vertical density structure is related to the vertical temperature structure. For now, we have made the approximation that the temperature $T(r,z)$ is independent of z for ease of calculation, which means $\partial c_s^2/\partial z = 0$, which is not entirely correct but not a terrible approximation, as the temperature gradient is usually small around the midplane, which is where most of the gas is located. The vertical hydrostatic balance is given by

$$\frac{\partial p}{\partial z} = -\rho\frac{GM_*}{r^3}z \equiv -\rho\Omega_K^2 z, \tag{29}$$

where we take $p = \rho c_s^2$ and the aforementioned assumption of $\partial c_s^2/\partial z = 0$, leading to

$$\frac{1}{\rho}\frac{\partial \rho}{\partial z} = -\frac{\Omega_K^2}{c_s^2}z. \tag{30}$$

The solution to this equation is

$$\rho(z) = \rho_0 \exp(-\frac{z^2}{2H^2}), \tag{31}$$

where H is the pressure scale height defined as $H \equiv c_s/\Omega_K$, which using the definition of the surface density can be rewritten as

$$\rho(z) = \frac{\Sigma}{H\sqrt{2\pi}} \exp(-\frac{z^2}{2H^2}). \tag{32}$$

We can use the definition of surface density, $\Sigma(r) = \int_{-\infty}^{+\infty} \rho(r,z)dz$, to rewrite the surface density as

$$\Sigma(r) = \rho_0 H\sqrt{2\pi}, \tag{33}$$

where ρ_0 is the midplane density and H the scale height. Both of these quantities depend on the radius r and temperature T. So we need an expression for the local temperature away from the midplane. For this, we need to consider viscous heating and stellar irradiation. Viscous heating is due to frictional forces due to differential rotation. The effective temperature from viscous heating is given by equation 28, where now we will refer to $T_{\rm disk}$ as T_{eff} because we will include other heating sources. We can relate the midplane temperature $T_{\rm accr}$ to the effective temperature using the vertical optical depth τ using

$$T_{\rm accr} = (\frac{3}{8}\tau)^{1/4} T_{\rm eff}. \tag{34}$$

Stellar irradiation heats surface layers of the disk. The irradiation temperature due to this effect is given by

$$T_{\rm irr}(r,z) = (\frac{\phi L_*}{r\pi\sigma r^2})^{1/4}, \tag{35}$$

where ϕ is the grazing angle of the incident stellar radiation, which depends on both the radius r and height z of the disk. and L_* the luminosity of the central host star. The total temperature $T(r,z)$ can then be obtained by combining the effects of accretion and irradiation, giving the relation

$$T(r,z) = (T^4_{\rm accr}(r,z) + T^4_{\rm irr}(r,z))^{1/4} \tag{36}$$

For this, we require information on the opacity of the disk, which is a mixture of dust and gas. Generally, dust opacity is much more important for the thermal structure of the disk, so we will focus solely on the dust opacity. This opacity is strongly frequency-dependent, as well as dependent on the composition and grain size of the dust. This gets very complicated quickly, so we differentiate between stellar wavelengths and IR. We use $\kappa_{\rm star}$ as the average opacity at stellar wavelength and κ_d as the average opacity of dust thermal emission. We define the dust-to-gas ratio as η and assume an approximate value of 0.01, which is not that different from what we use in equations 24 and 25. From this follows the vertical optical depth of the disk at dust-emission wavelengths:

$$\tau_d = \frac{1}{2}\Sigma\eta\kappa_d. \tag{37}$$

Using the same definitions for Ω_K, assuming an ideal gas, meaning $c_s = \sqrt{\frac{k_B T}{\mu m_p}}$, and using the definition of the scale height $H = \frac{c_s}{\Omega_K}$, we can obtain an expression for the scale height:

$$H(r) = \sqrt{\frac{k_B T r^3}{\mu m_p G M_*}}. \tag{38}$$

B SO_2-only mock spectra signal-to-noise analysis

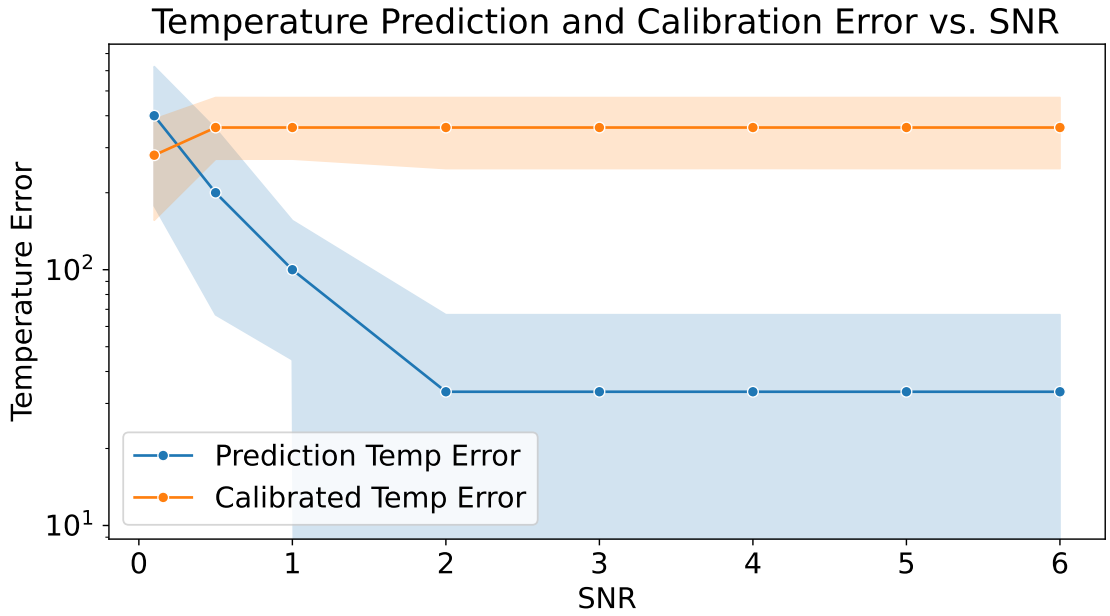

Figure 32: Calibration and prediction temperature versus the signal-to-noise ratio. The y-axis shows the mean offset between the true temperatures and the estimated temperatures of our sample spectra. The shaded region denotes the standard deviation of our 9 samples to the mean value shown.

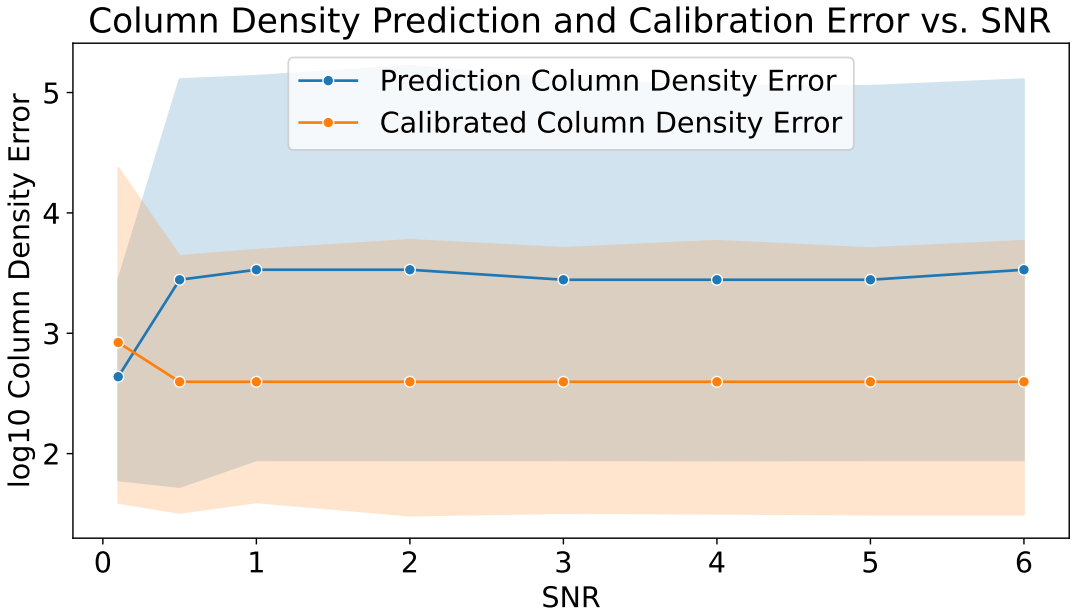

Figure 33: Calibration and prediction column densities versus the signal-to-noise ratio. The y-axis shows the mean offset between the true column densities and the estimated column densities of our sample spectra. The shaded region denotes the standard deviation of our 9 samples to the mean value shown.

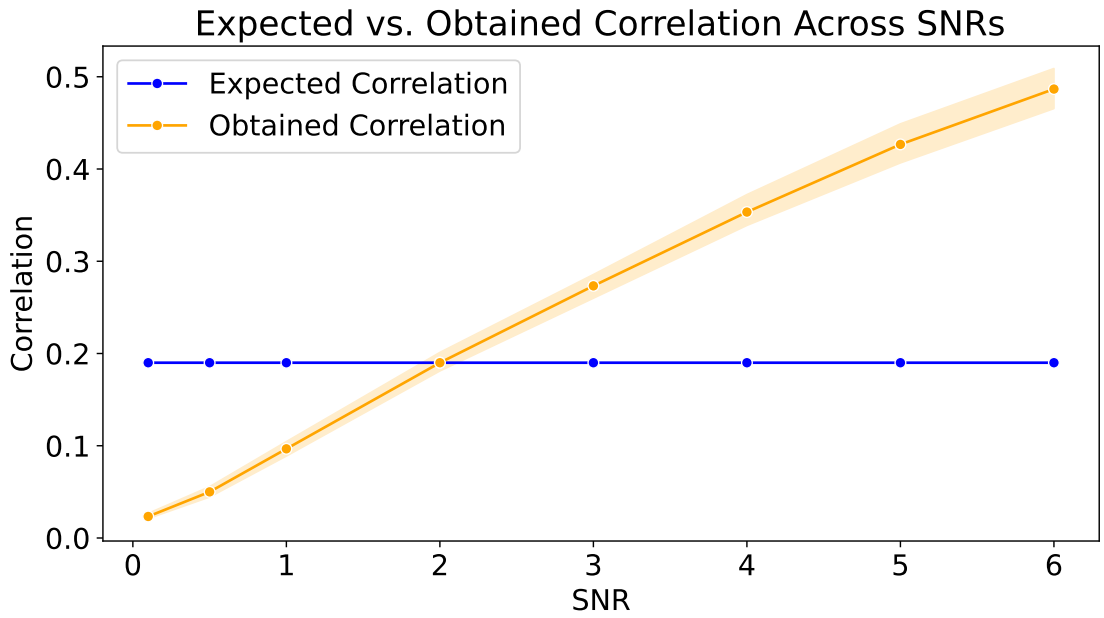

Figure 34: Expected and obtained correlations as a function of the signal-to-noise ratio. The expected correlation is the threshold above which we expect a valid measurement. The obtained correlation shows the mean correlation coefficient of our 9 sample spectra, with the shaded region denoting the standard-deviation.

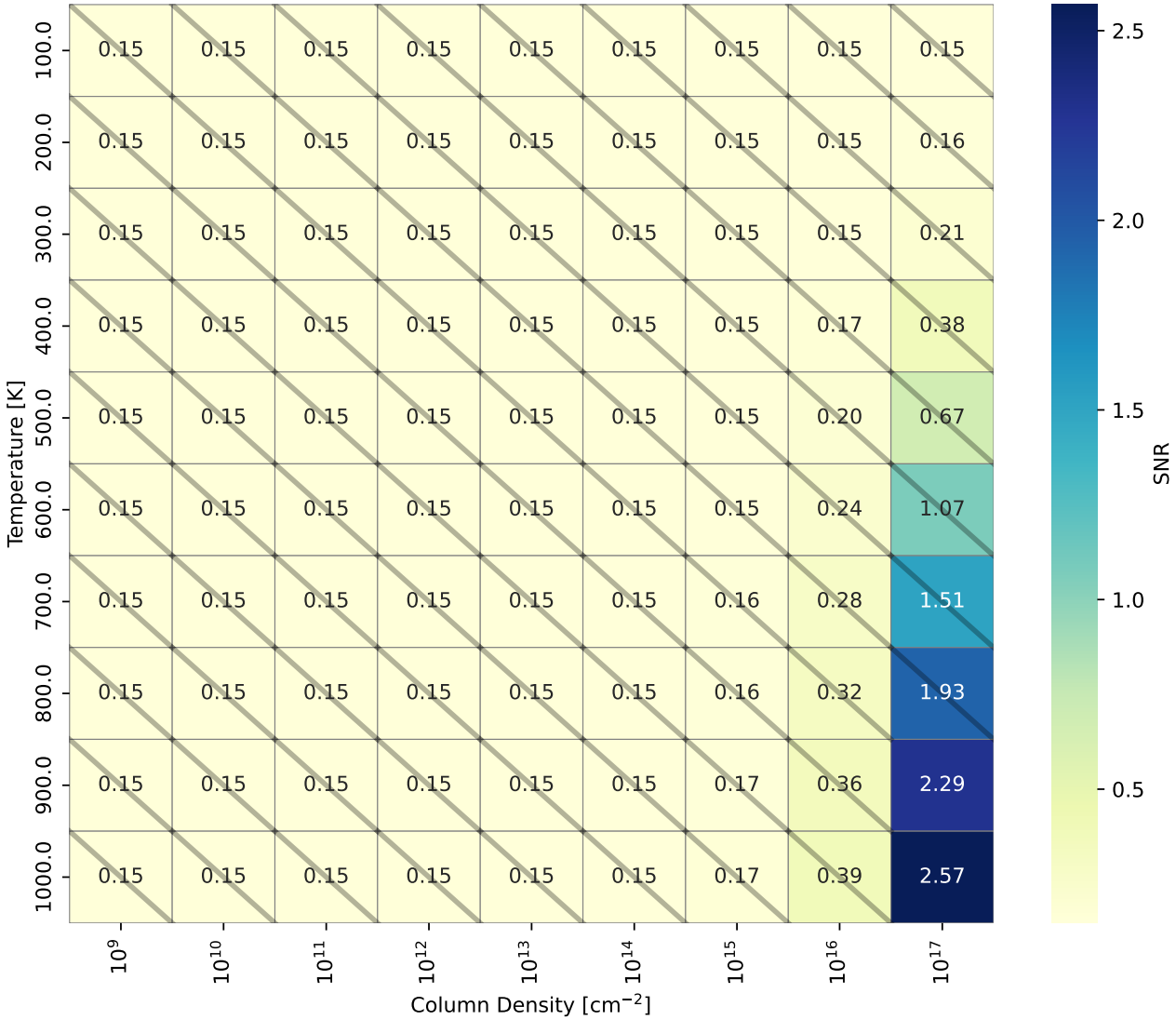

Figure 35: Signal-to-noise ratios obtained for different combinations of column density and temperature with an emitting radius of 0.1 AU. The diagonal stripes mark the models obtaining an SNR below the established threshold of 2.

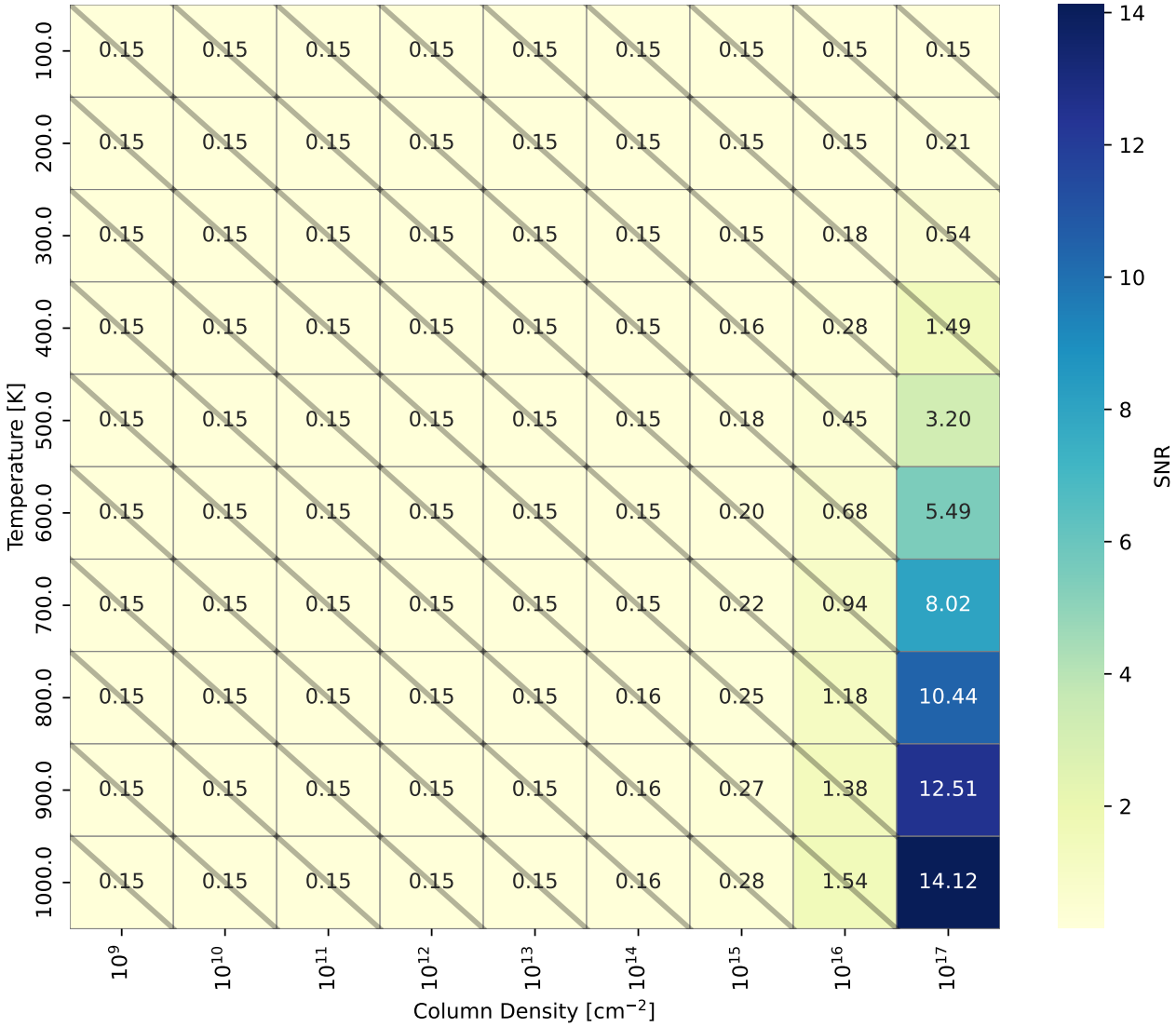

Figure 36: Signal-to-noise ratios obtained for different combinations of column density and temperature with an emitting radius of 0.3 AU. The diagonal stripes mark the models obtaining an SNR below the established threshold of 2.

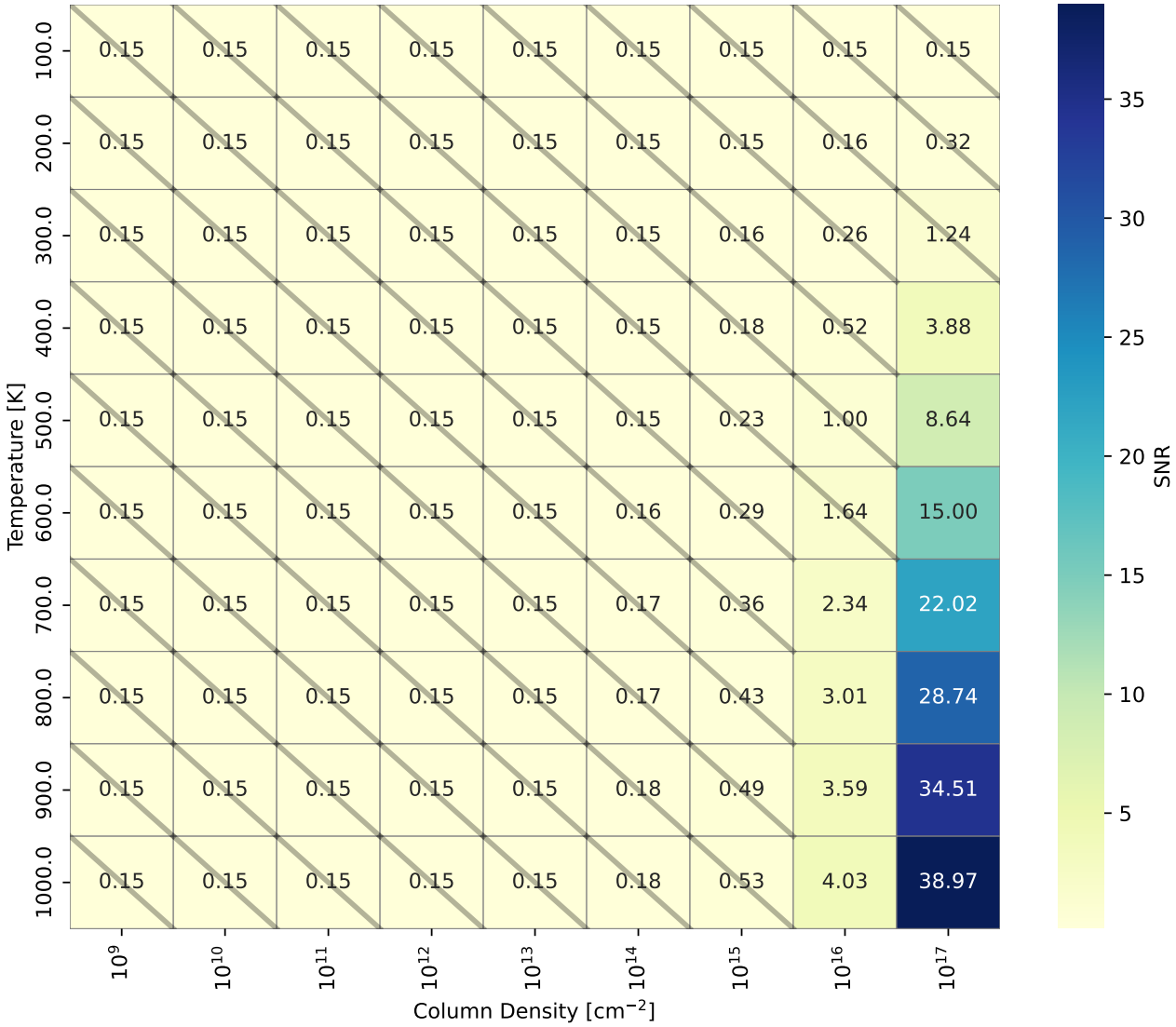

Figure 37: Signal-to-noise ratios obtained for different combinations of column density and temperature with an emitting radius of 0.5 AU. The diagonal stripes mark the models obtaining an SNR below the established threshold of 2.

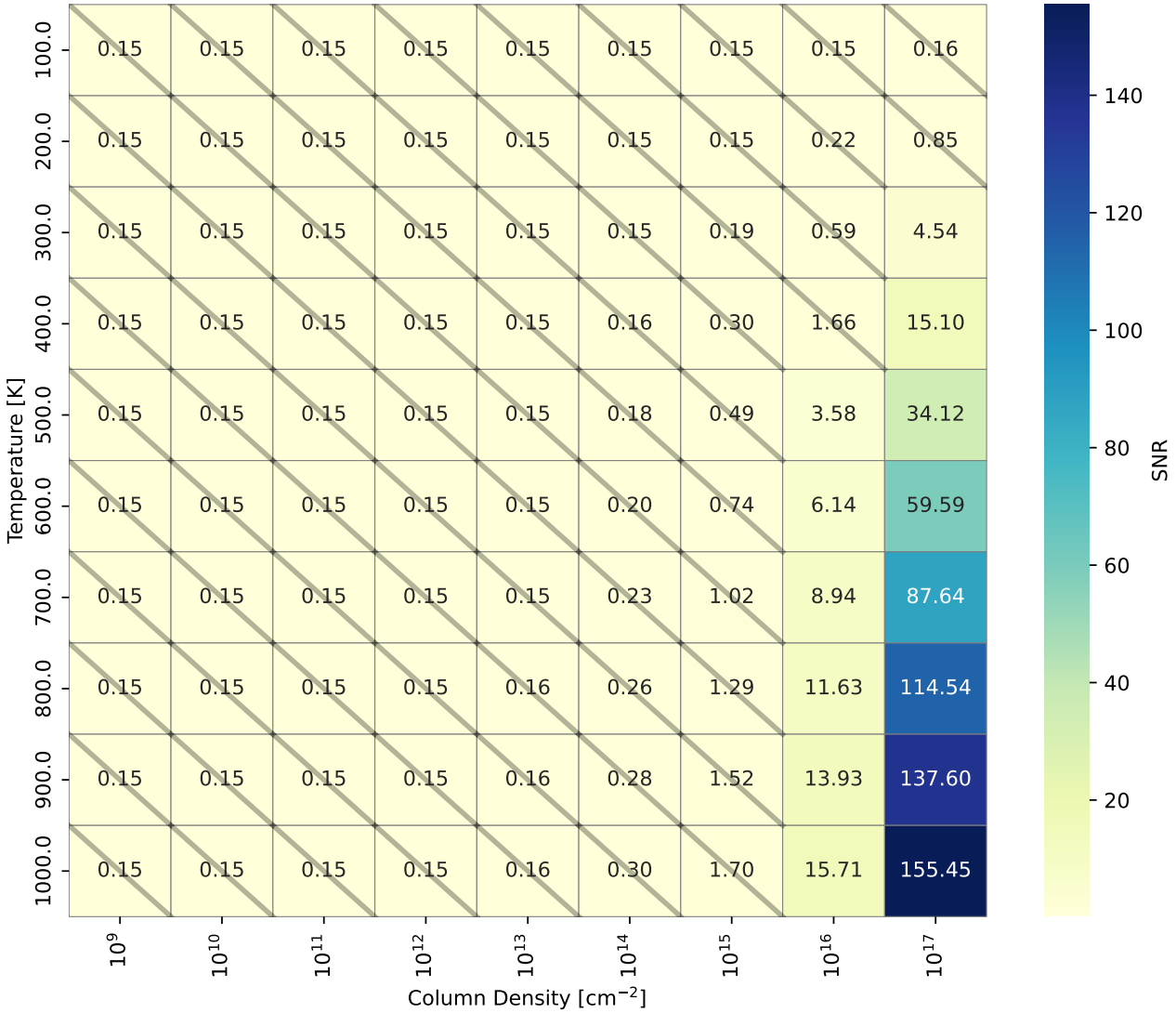

Figure 38: Signal-to-noise ratios obtained for different combinations of column density and temperature with an emitting radius of 1 AU. The diagonal stripes mark the models obtaining an SNR below the established threshold of 2.